## Title

On the use of charged particles to characterize precipitation in irradiated reactor pressure vessel steels with a wide range of compositions

**Authors**

Almirall, N
Wells, PB
Yamamoto, T
et al.

**Publication Date**

2020-08-01

**DOI**
10.1016/j.jnucmat.2020.152173

# On the Use of Charged Particles to Characterize Precipitation in Irradiated Reactor Pressure Vessel Steels with a Wide Range of Compositions

N. Almirall[1], P. B. Wells [1], T. Yamamoto[2], K. Yabuuchi[3] A. Kimura[3], G. R. Odette[1]
1) Materials Department, University of California, Santa Barbara, CA 93106, USA
3) Institute of Advanced Energy, Kyoto University, Kyoto, Japan

## Corresponding Author

G. Robert Odette
Distinguished Research Professor Emeritus, UCSB Mechanical Engineering and Materials Departments
Email: odette@engineering.ucsb.edu
Phone: (805) 964-5586
Fax: (805) 893-8651
Address:
Mechanical Engineering Department
2355 Engineering II
University of California, Santa Barbara
Santa Barbara, CA 93106-5070

## Abstract

Nuclear reactor lifetimes may be limited by nano-scale Cu-Mn-Ni-Si precipitates (CRPs and MNSPs) that form under neutron irradiation (NI) of pressure vessel (RPV) steels, resulting in hardening and ductile to brittle transition temperature increases (embrittlement). Physical models of embrittlement must be based on characterization of precipitation as a function of the combination of metallurgical and irradiation variables. Here we focus on rapid and convenient charged particle irradiations (CPI) to both: a) compare to precipitates formed in NI; and, b) use CPI to efficiently explore precipitation in steels with a very wide range of compositions. Atom probe tomography (APT) comparisons show NI and CPI for similar bulk steel solute contents yield nearly the same precipitate compositions, albeit with some differences in their number density, size and volume fraction (f) dose (dpa) dependence. However, the overall precipitate evolutions are very similar. Advanced high Ni (> 3 wt.%) RPV steels, with superior unirradiated properties, were also investigated at high CPI dpa. For typical Mn contents, MNSPs have $Ni_{16}Mn_6Si_7$ or $Ni_3Mn_2Si$ phase type compositions, with f values that are close to the equilibrium phase separated values. However, in steels with very low Mn and high Ni, $Ni_{2-3}Si$ silicide phase type precipitate compositions are observed; and when Ni is low, the precipitate compositions are close to the MnSi phase field. Low Mn significantly reduces, but does not eliminate, precipitation in high Ni steels. A comparison of dispersed barrier model predictions with measured hardening data suggests that the Ni-Si dominated precipitates are weaker dislocation obstacles than the G phase type MNSPs.

Key Words: Reactor Pressure Vessel Steels; Charged Particle Irradiation; Atom Probe Tomography; Irradiation Embrittlement; Nano-scale Precipitates; Thermodynamic Models

## 1. Introduction, Background and Objective

Extending the lifetime of nuclear plants to 80 years is critical to sustaining the world's largest contributor to C-free electricity production [1]. However, embrittlement of reactor pressure vessels may limit the extended lifetimes of light water nuclear reactors [2–4]. Embrittlement is primarily caused by nm-scale precipitates and solute-defect cluster complexes that evolve under irradiation [4–6]. Thermal precipitation at RPV operating temperatures around 290°C is very sluggish, but is greatly accelerated under irradiation by large excess populations of mobile vacancy and self-interstitial atom (SIA) defects. Precipitates that form by radiation enhanced diffusion (RED) and induced segregation (RIS) result in hardening (increases in the yield stress, $\Delta\sigma_y$), which in turn, cause embrittlement, manifested as an elevation in the steel's ductile to brittle transition temperature ($\Delta T$).

Life extension to 80 years will require robust predictions of RPV $\Delta T$ at high neutron fluence ($\phi t$), where power reactor surveillance data is largely unavailable [4,7–9]. Understanding microstructural evolutions as a function of $\phi t$, or displacements per atom (dpa), flux ($\phi$), irradiation temperature ($T_i$), product form and alloy composition, is needed for developing physically-based, predictive $\Delta T$ models [7–10]. High $\phi$ material test reactors (MTRs) have been extensively utilized to study RPV embrittlement because they can reach high $\phi t$ in a much shorter time than in a power reactor vessel [4,9]. Here we explore the potential of even more convenient charged particle irradiations (CPI) to study microstructural evolutions, with emphasis on the nanoscale precipitates. Limited comparisons show that CPI result in precipitate volume fractions (f) and compositions that are similar to those formed in neutron irradiations (NI). Thus, CPI were used here to characterize precipitation for a matrix of advanced alloys with compositions that extend beyond the typical range the current RPV steels. The focus is on developing so-called super-clean steels, with very high Ni contents (> 3 wt.%), that have superior unirradiated properties [11–16]. However, high Ni levels lead to enormous irradiation hardening and embrittlement in RPV steels with typical Mn and Si contents [11]. Thus, super-clean steels have much lower Mn (and impurity S) contents, which is aimed at limiting the amount of nanoscale precipitation. The CPI study reported here demonstrates that reductions in Mn do indeed reduce the precipitate f, but only to a limited extent. Notably, the CPI can easily reach several dpa resulting in a nearly fully phase separated precipitate volume fractions ($f_{max}$); while such high dpa are well above that experienced by vessels even during extended life, $f_{max}$is a necessary parameter in embrittlement models [4].

The main variables that interact to mediate $\Delta T$ are $\phi$, $\phi t$, $T_i$ and the Cu, Ni, Mn, Si and P contents of the steel [4–10]. Since RPV compositions vary widely around the world, accurate $\Delta T$ predictions require an understanding of the individual and synergistic effects of these variables. The earliest mechanistic embrittlement model was based on the rapid RED enhanced precipitation of Cu, as the dominant cause of hardening and embrittlement [17]. However, it was both observed and modeled early on, that Cu rich precipitates (CRPs) are alloyed with Mn, Ni and Si [10,18–21]. Copper is an impurity element in RPV steels and can remain dissolved up to concentrations ≈ 0.3 at.% [7,8,22]. Note, unless otherwise stated, compositions are expressed here in terms of at.%. In contrast to trace amounts of impurity Cu, the total concentration of alloying elements Ni, Mn and Si is typically ≈ 3 % or more. Thus, a major issue with RPV life extension is the potential the slow formation of much larger f of Mn, Ni and Si precipitates (MNSPs). Notably, the formation of MNSPs, even in low Cu steels, was first predicted about 25 years ago [10,18–21]. MNSPs can lead to unexpectedly severe hardening and corresponding $\Delta T$, but they are currently not accounted for in most regulatory models [4,7,8,23,24]. MNSPs, have been called late blooming phases (LBP), due to their slow nucleation and growth rates compared to CRPs [4–6,9–11,18–21]. However, MNSPs are now widely observed [25–35]. Further, recent models [36–39] support the early predictions of their evolutions as intermetallic phases. While MNSPs form in low Cu steels, primarily by heterogeneous nucleation [36,37], they also emerge as separate appendage co-precipitates, attached to CRP core shell structures at high $\phi t$ [4,31,33,39,40]. The main driver for MNSP formation is Ni. The MNSPs are nearly completely precipitated at very high neutron $\phi t$, predicted by Fe-Mn-Ni-Si system phase boundaries, as modified by the Gibbs-Thomson effect; for example in a high $\phi t$ study, the MNSP f was $\approx 0.75(2\mathrm{Ni} + \mathrm{Cu}) + 0.27$ [4,11,31,33].

However, neutron irradiations (NI) of RPV steels to study embrittlement at high, extended life $\phi t$ are costly and time-consuming. In contrast, charged particle irradiations (CPI) can be used to rapidly explore the effects of embrittlement variables and mechanisms, typically taking tens of hours to produce 80-year NI damage doses, in units of dpa [41–43]. The charged particle is typically a medium weight ion like $\mathrm{Fe}^{++}$. Heavy ion CPI do not produce radioactive byproducts, thus samples can be handled without any special safety procedures. While they do not simulate neutron embrittlement, CPI provide a rapid and cost effective way to gain insight into precipitation mechanisms. Further, CPI can help to determine which new RPV steel compositions are most likely to be susceptible to the formation of large f of MNSPs, thus helping to guide future advanced RPV steel development.

However, there are many differences between NI and CPI as noted in the partial list and dpa rates can strongly affect RED accelerated precipitation [4–6,9,25,31,33,37,38,43–46]. For example, for a fixed set of other variables, far fewer defects escape vacancy-SIA recombination at high dpa rates, thereby reducing the efficiency of RED and defect accumulation. RIS driven precipitation also depends on damage rate, as do the effects of ballistic mixing [46,47]. Further, there are differences between CPI and NI secondary atomic recoil spectra [41]. CPI effects are modified by nearby free surface defect sinks, and experience steep depth gradients in dpa and dpa rates [41,42]. Local dpa rates are also time dependent if the ion beams are rastered [42]. CPI injects extra interstitials of the bombarding species [41,42]. Finally, accelerator irradiations can also lead to impurity pickup of elements like C [48,49].

Thus one objective of this work was to compare the precipitates formed in RPV steels in both NI and CPI irradiated conditions. This comparison showed that, in general, the differences are moderate. Specifically we directly compare the precipitate average diameters (<d>), number densities (N), f and compositions for steels with: a) high 0.24 % Cu and 1.03 % Ni (LD) and a medium 0.15 % Cu and 0.71 % Ni (LI) following CPI at ≈ 290°C and NI at ≈ 300°C, both to ≈ 0.2 dpa; b) the same LD alloy NI at 320°C to a high ≈ 1.8 dpa, and CPI irradiated at 290°C to an even higher ≈ 4.0 dpa. While direct comparisons were not possible in the following cases, two other NI low < 0.02 % Cu steels, with medium 0.69 % Ni (LG) and high 1.71% % Ni (CM6), and 1.15±0.28 Mn contents, were compared to two other low <0.05 % Cu CPI steels with roughly similar respective Ni and Mn compositions (A39 ≈ 0.57 % Ni, ≈ 0.91 Mn and A22 ≈ 1.82 % Ni, 1.28 % Mn). Again, the NI was ≈ 1.8 dpa at 320°C and the CPI was at 290°C to ≈ 4.0 dpa. Note, these A-series steels were also NI in a lower ≈ 0.2 dpa, 290°C irradiation, but comparable dpa CPI data on these alloys is not available. In all cases only a modest differences in composition of the MNSPs was observed. The MNSP f was slightly lower in the CPI condition, which is not unexpected due to the high dpa rate, while the corresponding N values are lower and the <d> are somewhat larger.

A second objective of this study was to characterize and analyze the precipitates in new very high Ni (> 3 %) alloys formed under CPI as a function of the combined effects of Ni, Mn and Si. The precipitate <d>, N and f values generally increase with Mn, Si, Cu and, especially, Ni. More notably, however, the MNSP f increases linearly with the G phase solute product $SP_G = [Ni^{16}Mn^{6}Si^{7}]^{1/29}$.

The paper is structured as follows. Section 2 describes the experimental materials and methods. Section 3.1 demonstrates the ability of CPI to produce MNSPs with similar f and compositions as NI. Supported by these results, Section 3.2 summarizes the effects of high dpa CPI on MNSPs in the advanced steel (A-series) matrix with a wide range of compositions, including high Ni. Section 3.3 describes a thermodynamic analysis of these results. Section 3.4 estimates the irradiation $\Delta\sigma_y$ and $\Delta T$ in the CPI at in both nearly fully precipitated and lower dpa NI relevant service conditions. Finally, Section 4 summarizes the overall results.

## 2. Experimental Methods

The compositions and heat treatments of the RPV steels in this study are shown in Table 1. The small heat, split-melt steels have microstructures and mechanical properties that are essentially the same as actual RPV steel base metals with similar compositions.

Table 1. Nominal steel compositions (at.%)

| Alloy | Bulk at.% | | | | | | | | |
|---|---|---|---|---|---|---|---|---|---|
| | Cu | Ni | Mn | Si | Cr | Mo | P | C | Fe |
| LG* | <0.01 | 0.70 | 1.38 | 0.43 | 0.05 | 0.32 | 0.01 | 0.74 | Bal. |
| CM6* | 0.02 | 1.59 | 1.52 | 0.34 | 0.05 | 0.31 | 0.01 | 0.69 | Bal. |
| LD* | 0.33 | 1.18 | 1.39 | 0.45 | 0.07 | 0.31 | 0.01 | 0.88 | Bal. |
| LI* | 0.17 | 0.70 | 1.38 | 0.47 | 0.09 | 0.32 | 0.01 | 0.74 | Bal. |
| A13† | 0.06 | 3.28 | 1.49 | 1.24 | 0.11 | 0.30 | 0.01 | 1.06 | Bal. |
| A16† | 0.52 | 3.27 | 1.52 | 0.40 | 0.11 | 0.30 | 0.01 | 1.02 | Bal. |
| A22† | 0.05 | 1.58 | 1.51 | 0.41 | 0.11 | 0.30 | 0.01 | 1.34 | Bal. |
| A28† | 0.05 | 3.26 | 0.25 | 1.22 | 0.11 | 0.31 | 0.01 | 1.24 | Bal. |
| A32† | 0.05 | 3.34 | 2.08 | 0.45 | 0.14 | 0.30 | 0.02 | 1.02 | Bal. |
| A34† | 0.06 | 3.25 | 0.08 | 0.38 | 0.10 | 0.28 | 0.01 | 1.02 | Bal. |
| A37† | 0.05 | 0.20 | 1.49 | 1.22 | 0.11 | 0.30 | 0.01 | 1.24 | Bal. |
| A39† | 0.03 | 0.66 | 1.47 | 0.41 | 0.12 | 0.28 | 0.01 | 0.97 | Bal. |

* Also contains some S and other trace elements. L-series heat treatment: austenized at 900°C for 1 h, air cooled, tempered at 664°C for 4 h, air cooled, stress relieved at 600°C for 40 h, followed by a furnace cooling to 300°C, then air cooled to room temperature. CM heat treatment: tempered at 660°C for 4 h, air cooled, then stress relieved at 607°C for 24 h followed by a slow cool at 8°C/h to 300°C, then air cooled

† A series matrix heat treatment: austenitized at 920°C for 1 h followed by an air cool, then tempered at 600°C for 5 h followed by an air cool.

The NI were carried out in the Belgian Reactor 2 (BR2) at a $\phi \approx 1.0x10^{14}$ n/cm$^2$-s to a $\phi t \approx 1.3x10^{20}$ n/cm$^2$ at 300°C [50]; and the Advanced Test Reactor (ATR) at Idaho National Laboratory at a $\phi \approx 2.3x10^{14}$ n/cm$^2$-s to a $\phi t \approx 1.1x10^{21}$ n/cm$^2$ at 320°C [51,52]. This $\phi t$ corresponds to $\approx$ 0.2 dpa and $1.4x10^{-7}$ dpa/s and $\approx$ 1.8 dpa and $3.1x10^{-7}$ dpa/s, respectively. These results of these have been partially published previously [31,33]. The target temperature of this irradiation location was 290°C. However, the final INL "as run" irradiation temperature was revised to be $\approx$ 320°C as reported in [51]. The CPI were carried out at the Dual Beam Facility for Energy Science and Technology (DuET) at Kyoto University in Japan. A rastered beam of 6.4 MeV $Fe^{3+}$ ions produced a peak of 0.6 or 13 dpa at 290°C and a depth of $\approx$ 1.6 μm in 3.0 mm diameter x 0.5 mm thick disc specimens. The Kinchin-Pease model in the SRIM 2008 code, with a displacement energy of 40 eV, was used for the dpa calculation, as recommended in ASTM E521-96 (2009) [53]. The dpa rate at the APT sampling depth was about ≈ $3.4\text{x}10^{-5}$ and ≈ $1.5\text{x}10^{-4}$ dpa/s. The sample temperature was controlled using infrared heater on the back of specimen stage and a thermal imaging camera to monitor at the front of the specimens, calibrated with K-type thermocouple measurements on a dummy steel sample. The uncertainty in the irradiation temperature is estimated to be ≈ ± 5°C. The ion beam in the DuET facility is rastered at 300 and 1000 Hz vertically and horizontally, respectively.

Figure 1a shows the Focused Ion Beam (FIB) liftouts, which subsequently were sharpened by annular milling to fabricate APT needles with a tip radius of ≈ 50-100 nm. The FIB voltages and beam currents were reduced to 5 kV and 48 pA and 2 kV and 27 pA, respectively, for final cleanup and partial removal of Ga damage layer. Procedures for creating site-specific liftouts and sharpened APT tips by annular milling are described elsewhere [54,55]. The 5 kV cleanup milled the tip to ≈ 500 +/- 50nm depth from the top liftout surface, corresponding to ≈ 0.2 dpa at ≈ $3.4\text{x}10^{-5}$ dpa/s and ≈ 4.0 dpa at ≈ $1.5\text{x}10^{-4}$ dpa/s. Figure 1b shows that at the higher dpa rate the damage profile gradient in this region modest, varying from ≈ 4.0-4.4 dpa over the 150 nm depth sampled. The irradiation conditions are summarized in Table 2. We refer to the low and higher dpa rate CPI irradiations as DuET:L and DuET:H, respectively.

**Figure 1.**

Table 2. NI and CPI conditions.

| Facility | dpa | Particle | Energy (MeV) | $\phi t$ (n-cm$^{-2}$) | Neutron $\phi$ (n-cm$^{-2}$s$^{-1}$) | Dose (dpa) | Dose/dpa Rate (dpa/s) | $T_{irr}$ (°C) |
|---|---|---|---|---|---|---|---|---|
| BR2 | Low | Neutron | >1 | $1.3 \times 10^{20}$ | $1.0 \times 10^{14}$ | 0.2 | $1.4 \times 10^{-07}$ | 300 |
| ATR1 | High | Neutron | >1 | $1.1 \times 10^{21}$ | $2.3 \times 10^{14}$ | 1.8 | $3.1 \times 10^{-07}$ | 320 |
| DuET:L | Low | $Fe^{3+}$ | 6.4 | - | - | 0.2 | $3.4 \times 10^{-05}$ | 290 |
| DuET:H | High | $Fe^{3+}$ | 6.4 | - | - | 4.0 | $1.5 \times 10^{-04}$ | 290 |

Atom Probe Tomography (APT) was used to characterize the volume fraction (f), diameter (d), average diameter (<d>), number density (N), and precipitate composition [30,31,56–58]. The high dpa NI specimens were examined using a Cameca LEAP 4000X HR at the Idaho Center for Advanced Energy Studies (CAES) while the ion irradiated specimens were run in a CAMECA LEAP 3000X HR at the University of California, Santa Barbara (UCSB). The specimens were run in voltage mode, which utilized identical systems within the LEAP 3000-4000 X HR, at a target evaporation rate of 0.50%, a pulse repetition rate of 200 kHz with a 20% pulse fraction and a specimen temperature of $\leq$ 50K.

The reconstructions were performed with the CAMECA Integrated Visualization and Analysis Software (IVAS v3.6.12). Planes within low index poles were used to depth scale the reconstruction [59]. The cluster analysis was performed using the core-linkage algorithm, an extension of the maximum separation method, in the IVAS reconstruction package, as described elsewhere [60–62]. Based on a sensitivity analysis the following parameters were consistently used: order = 5; $d_{max}$=0.50-0.65 nm, $N_{min}$=15-65 and maximum separation envelope of additional elements (L) = erosion distance of matrix elements ($d_{er}$) $<=$ $d_{max}$. Further information on and improvements made to selection of cluster parameters can be found elsewhere [63]. The ranged solutes were Cu, Mn, Ni and Si and the overlapping Fe/Ni peak at 58 Da was initially ranged as Ni, but a correction was then made to the number of Fe and Ni atoms using abundance ratios for Ni and Fe isotopes, as discussed elsewhere [11]. The N was calculated by dividing the total number of clusters within the tip by the total sampled tip volume; the volume was calculated from the number of atoms evaporated multiplied by the atomic volume of Fe and corrected for detector efficiency. The efficiency corrected number of solute atoms in a cluster, multiplied by the atomic volume of Fe, is used to determine the corresponding spherically equivalent volume. The radius of that volume was then determined and the volume weighted average radius was then calculated. Clusters that were determined to be on the edge of the sample were counted as 0.5 in the N calculation and were excluded from the average size calculation. The precipitate mole fraction was calculated by dividing the number of solute atoms in the clusters by the total number of atoms in the probed region of the APT tip.

Despite being a powerful characterization tool, APT suffers from a number of potential artifacts such as surface diffusion, trajectory aberrations, multiple hits, pre-emission and variations in the local magnification factor [33,45,64–66]. While these artifacts can be minimized through carefully selected run parameters and advanced reconstruction procedures, they complicate the analysis. Trajectory aberrations (TA) refers to the changes in the local magnification factor relating to the tip topology [33,58,61,66,67]. Lower (in relation to the predominantly Fe matrix) evaporation field features like CRPs and MNSPs, result in local flattening, or even dimpling of the tip [64,68]. This change in local magnification causes the matrix atoms to focus into the detector region containing the precipitate atoms. In turn this results in the erroneous measurements of the precipitate composition and the appearance of physically unrealistic high hit densities of atoms within the precipitate [33,58]. By combining STEM-EDS and multi technique characterization studies (small-neutron scattering, small-angle X-ray scattering, positron annihilation coincidence Doppler broadening, orbital electron momentum spectrum and lifetime measurements and combined electrical resistivity and Seebeck coefficient measurements), it’s been clearly shown high concentrations of Fe in the precipitates are an APT artifact [45,64]. Thus the Fe content within the precipitates was excluded from calculations of precipitate size and compositions [33,45,64,66]. Further details on the methods of analysis can be found elsewhere [11,31,33,69].

## 3. Results and Discussion

### *3.1 APT Comparisons of the NI and CPI Precipitates*

Figure 2 shows solute APT maps directly comparing the 0.15 % Cu and 0.71 % Ni, (LI) and the 0.24 % Cu and 1.03 % Ni (LD) steels that were NI and CPI at 295±5°C to ≈ 0.2 dpa. We have reported elsewhere [31] that the precipitates track the local composition that varies from tip to tip. Thus the compositions and f are the corresponding averages. Unless otherwise noted, the steels in section study contain ≈ 1.04±0.17 % Mn and ≈ 0.45±0.1 % Si. The relatively homogeneous distribution of quasi-spherical precipitates is qualitatively similar for both irradiation conditions in both alloys. Table 3 and Figure 3 show the precipitate Mn, Ni and Si compositions in both the CPI and NI conditions are nearly the same for both the LD (25.9±3.8 %Cu, 36.9±0.9 %Ni, 21.3±3.3 %Mn and 15.9±0.4 %Si) and LI (23.2±1.0 %Cu, 35.2 ±1.0 %Ni, 25.3±2.2 %Mn and 16.4±2.2 %Si) steels. The Si is only slightly higher and Mn slightly lower in the CPI condition. Table 4 shows that the main differences are a higher N and f in the NI condition, especially for the lower Cu and Ni steel. Figure 4 cross plots <d>, N and f for both steels in the two-irradiation conditions as a function of the bulk Cu in individual tips (again note, Ni also varies); <d> increases slightly with increasing Cu (and Ni), but is similar for the NI and CPI conditions; N and f also increase with Cu (and Ni). These results are qualitatively consistent with trends observed in previous NI studies of Cu bearing RPV steels, showing a large number of CRPs, either with a Mn, Ni and Si shell, or with a MNSP appendage [4,11,31]. The larger f in the NI condition is expected due to the much higher CPI dpa rate, which reduces the efficiency of RED. One *seeming* exception to previously observed NI trends, is a lower N for the higher dpa rate CPI case. At lower dpa, the precipitate N generally increases with NI flux, or dpa rate. However, closer analysis of the NI data shows that this lower dpa trend is not observed at very high dpa and dpa rates (see Figure 10 below). Thus the lower CPI N is actually consistent with the high NI dpa trends.

**Figure 2.**

**Figure 3.**

Table 3. Bulk, matrix and precipitate Cu, Ni, Mn and Si compositions at the lower and high dpa in the CPI (DuET:L and DuET:H) and NI (BR2 and ATR1) conditions. The absolute bulk and matrix compositions obtained from APT measurements are in at. %, while those for the precipitates are specified in terms of fractional %.

| Alloy | Bulk Comp. (at.%) | | | | Matrix Comp. (at. %) | | | | Precipitate Composition (fractional %) | | | |
|---|---|---|---|---|---|---|---|---|---|---|---|---|
| | Cu | Ni | Mn | Si | Cu | Ni | Mn | Si | Cu | Ni | Mn | Si |
| LD:BR2 | 0.21 | 1.00 | 1.08 | 0.52 | 0.06 | 0.74 | 0.91 | 0.41 | 22.1 | 37.8 | 24.6 | 15.5 |
| LD:DuET:L | 0.26 | 1.06 | 1.17 | 0.54 | 0.11 | 0.88 | 1.08 | 0.46 | 29.7 | 36.0 | 18.0 | 16.3 |
| LI:BR2 | 0.15 | 0.72 | 1.21 | 0.43 | 0.06 | 0.59 | 1.11 | 0.37 | 24.2 | 34.2 | 27.4 | 14.2 |
| LI:DuET:L | 0.15 | 0.70 | 1.21 | 0.44 | 0.11 | 0.64 | 1.19 | 0.41 | 22.2 | 36.2 | 23.1 | 18.5 |
| LD:ATR1 | 0.25 | 1.18 | 1.08 | 0.54 | 0.04 | 0.21 | 0.57 | 0.08 | 10.3 | 46.9 | 22.5 | 20.3 |
| LD:DuET:H | 0.23 | 1.22 | 1.12 | 0.54 | 0.10 | 0.29 | 1.24 | 0.17 | 8.5 | 50.2 | 20.9 | 20.4 |
| LG:ATR1 | 0.00 | 0.71 | 0.87 | 0.43 | 0.00 | 0.11 | 0.38 | 0.10 | 0.2 | 46.1 | 31.2 | 22.5 |
| A39:DuET:H | 0.03 | 0.57 | 0.91 | 0.36 | 0.02 | 0.19 | 0.61 | 0.17 | 0.8 | 47.0 | 29.3 | 22.9 |
| CM6:ATR1 | 0.00 | 1.69 | 1.42 | 0.39 | 0.00 | 0.21 | 0.31 | 0.04 | 0.1 | 52.5 | 35.5 | 11.9 |
| A22:DuET:H | 0.05 | 1.82 | 1.28 | 0.51 | 0.03 | 0.46 | 0.75 | 0.10 | 0.9 | 57.5 | 23.9 | 17.7 |

Table 4. Bulk Cu, Ni, Mn and Si compositions and APT precipitate <d>, N and f at the low and high dpa in the CPI (DuET:L and DuET:H) and NI (BR2 and ATR1) conditions.

| Alloy | Bulk Composition (at.%) | | | | <d> | +/- | N | +/- | f | +/- | $10^6$ ions |
|---|---|---|---|---|---|---|---|---|---|---|---|
| | Cu | Ni | Mn | Si | (nm) | (nm) | ($10^{23}$ m$^{-3}$) | ($10^{23}$ m$^{-3}$) | (%) | (%) | $10^6$ |
| LD:BR2 | 0.21 | 1.00 | 1.08 | 0.52 | 2.23 | 0.12 | 11.7 | 1.87 | 0.68 | 0.10 | 78.8 |
| LD:DuET:L | 0.26 | 1.06 | 1.17 | 0.54 | 2.28 | 0.07 | 7.49 | 1.17 | 0.46 | 0.06 | 28.1 |
| LI:BR2 | 0.15 | 0.72 | 1.21 | 0.43 | 2.19 | 0.11 | 6.89 | 1.14 | 0.37 | 0.08 | 14.1 |
| LI:DuET:L | 0.15 | 0.70 | 1.21 | 0.44 | 2.02 | 0.11 | 3.42 | 0.87 | 0.13 | 0.01 | 16.0 |
| LD:ATR1 | 0.25 | 1.18 | 1.08 | 0.54 | 4.01 | 0.31 | 6.98 | 1.26 | 2.11 | 0.23 | 40.8 |
| LD:DuET:H | 0.23 | 1.22 | 1.12 | 0.54 | 4.65 | 0.39 | 3.33 | 0.32 | 1.97 | 0.32 | 160.0 |
| LG:ATR1 | 0.00 | 0.71 | 0.87 | 0.43 | 2.54 | 0.10 | 15.5 | 1.61 | 1.33 | 0.03 | 26.5 |
| A39:DuET:H | 0.03 | 0.57 | 0.91 | 0.36 | 4.05 | 0.30 | 3.26 | 0.13 | 0.91 | 0.40 | 14.9 |
| CM6:ATR1 | 0.00 | 1.69 | 1.42 | 0.39 | 3.18 | 0.09 | 17.3 | 1.32 | 2.82 | 0.14 | 30.0 |
| A22:DuET:H | 0.05 | 1.82 | 1.28 | 0.51 | 4.99 | 0.35 | 4.85 | 0.62 | 2.40 | 0.39 | 31.5 |

**Figure 4.**

Figure 5 shows the APT maps for the same high 0.24±0.02 % Cu and 1.20±0.02 % Ni steel (LD) in the high ≈ 1.8 dpa, 320°C NI and ≈ 4.0 dpa, 290°C CPI conditions. The corresponding MNSP parameters, summarized in Tables 3 and 4, again show that in the NI condition the N values are larger, while the <d> are slightly smaller. However, the MNSP f (1.97-2.11%) and compositions (9.4±0.9 %Cu, 48.6±1.7 %Ni, 21.7±0.8 %Mn and 20.4±0.05 %Si) are nearly identical. In both cases the alloy is nearly completely precipitated. Note the small N and <d> differences may partly be due to the higher NI $T_i$.

Figure 6 shows APT maps comparing high dpa NI and CPI conditions for the LG/A32 and CM6/A22) steels with low Cu, and both medium ≈ 0.64$\pm$0.07 (LG/A32)) and high ≈1.76$\pm$0.06 %Ni (CM6/A22). These steels also contain 0.87 to 1.42 % Mn and 0.36 to 0.51 % Si. The <d>, N and f cross plots in Figures 7a-c are for individual tips of high Cu and Ni steel (LD). The CPI alloys have distinctly lower N and slightly lower f compared to the NI results. The CPI <d> values are also slightly larger; and the N and f increase with Cu in both irradiation conditions. These trends are similar to those in the same steel at lower dpa. Figures 7d-f show the corresponding comparison for low Cu and both low and high Ni steels with roughly similar Mn and Si contents. The <d>, N and f all increase with Ni, in a way that is similar for both the NI and CPI conditions. If thermodynamic solute product based adjustments (see Section 3.3) are made to account for differences in the Mn, Ni and Si in the medium Ni LG/A32 and high Ni CM6/A22 alloys, the f for the NI condition (1.8 dpa at 320°C) are about 13% (medium Ni) to 33% (high Ni) larger than for the CPI condition (4 dpa at 290°C). Again, this observation is consistent with slower precipitation at a higher dpa rate.

Figure 8a shows the MNSP fractional compositions are also similar in the paired LG/A39 and CM6/A22 steels, again especially if differences in the bulk alloy compositions are considered. The MNSP compositions in the high Ni alloys average Ni ≈ 55±2.5, while the Mn + Si ≈ 45±.3.0; in the medium Ni steel the MNSP compositions average Ni ≈ 47±0.5, while the Mn + Si ≈ 53±1.0%. As a compliment to Figure 8a, the stacked bar graph in Figure 8b shows the absolute individual volume fractions of the Mn, Ni and Si solutes in both the bulk steels and precipitates. Here, Cu is excluded since it is a separate attached phase. Figure 8b shows that: a) as expected, significant amounts of solutes remain dissolved in the matrix; b) the absolute f of the DuET CPI are smaller than for the ATR-1 NI, especially when adjusted for the bulk solute contents; and c) the largest difference in the CPI versus NI relative precipitate compositions is the somewhat lower amount of Mn in A22 versus CM6 (also see Figure 8a), but this tracks similar differences in the bulk solute content.

**Figure 5.**

**Figure 6.**

**Figure 7.**

**Figure 8.**

Figure 9a-d shows APT map blowups of the CPI and NI precipitates in the high Cu-Ni content steel (LD) for both the low and high dpa conditions. At a lower 0.2 dpa the precipitates exhibit a core-shell structure in both CPI and NI conditions. At high dpa the Cu-rich core grows a MNSP appendage in both cases, consistent with previous high dpa NI observations [31,38,39]. The blown up view Figure 9e for the high 3.69 Ni and 1.31 Si alloy with 0.98 Mn (A13) in the high dpa DuET:H CPI condition, suggests that the MNSP is a compact polyhedral intermetallic precipitate.

Clearly, NI and CPI produce similar precipitate microstructures. In a given alloy, the major differences are lower N and f and slightly larger <d> (at high dpa) in the CPI condition. While increasing N at higher dpa rate has often been observed in lower dpa NI, Figure 10 shows that N actually decreases with dpa for the CPI in a way that is close to the extrapolated trend for a NI alloy at high $\phi > 10^{13}$n/cm$^2$-s (1.6x10$^{-8}$ dpa/s) and $\phi t > 10^{20}$ n/cm$^2$ (0.15 dpa). While this trend is opposite to those observed for NI at lower dpa rates and dpa, it is qualitatively consistent with the effect of ballistic mixing by cascades [47]. Nevertheless, in view of these modest differences, CPI can be used as a convenient tool to assess the relative embrittlement sensitivity to various steel compositions, as well as a way to create RPV steel precipitate microstructures for scientific studies of mechanisms. It should be emphasized that these conclusions are for modest dpa and dpa rate CPI irradiations. This degree of NI and CPI similitude may not be the case for much higher CPI dpa and dpa rates used in studies of phenomena like void swelling and irradiation effects in Fe-Cr steels for advanced reactor applications.

**Figure 9.**

**Figure 10.**

### *3.2 Characterization of Precipitation in the DuET CPI Steels*

The APT solute maps in Figure 11 for the 6 advanced steel series (A-series) CPI at 4 dpa and 290°C (not shown previously) that contain a wide range of 0.19 to 3.69 %Ni, 0.03 to 0.25% Cu, 0.08 to 1.21% Mn, and 0.36 to 1.31% Si. The APT maps, precipitate parameters and compositions in Tables 5 and 6 reveal the effects of systematic variation in bulk solute contents. Figure 12a and Table 6 shows a very high Ni and Si (3.23 Ni 0.98 Mn 1.26 Si %) A13 steel, with the largest total solute content of ≈ 5.47 % in the A-series CPI alloys, contains a very large MNSP f ≈ 4.51%, even without much Cu. Note the Ni/Mn/Si phase composition, of ≈ 61/14/25, is reasonably close to the stoichiometric G-phase ($Ni_{16}Mn_6Si_7$ - 55/21/24), but with a higher Ni and Si contents, reflecting the larger alloy content of these elements.

Figure 11b shows the APT maps for a medium 0.45 % Si, high 3.1 % Ni (A32). Both alloys contain relatively high 0.98 (A13) and 1.26 (A32) % Mn. As expected that both the Si content and f of the MNSPs are lower in A32 compared to the high Si steel (A13). Table 6 shows that f decreases from 4.51 to 3.83% between A13 and A32, primarily associated with a lower N. The Ni contents of the MNSPs (61.9 and 65.9%) are similar. Thus, in spite of large differences in alloy Si (A32 0.45 and A13 1.26 %) the total MNSP percentages of Mn + Si (A13 33.5% and A32 38.6%) are also similar, since they trade off with each other, as observed previously in lower dpa NI study [11].

Figure 11c shows the MNSPs in a high 3.69 Ni and 1.31 Si % alloy with low 0.29 % Mn (A28). Table 6 shows that f decreases slightly from ≈ 4.51 to 3.95% between alloy contents of 0.98 (A13) and 0.29 % Mn (A28). The lower f can be attributed to less Mn (5.00 versus 13.9%) in the A28 MNSPs. In both cases, Ni-Si rich MNSPs have compositions about midway between $Ni_2Si$ and $Ni_3Si$ type phases. Note that some individual tips of A28 steel contain atypically high bulk Ni, producing higher f than on average.

Figure 11d shows that CRP/MNSP co-precipitates form in the high 0.25 % Cu steel with high Ni, Mn and Si (A16). CRPs, with a Cu-rich core and Mn-Ni-Si shell, form rapidly then slowly evolve discrete, what appears to be an ordered intermetallic co-precipitate appendages at higher dpa (see Figure 8) [31,39]. CRP/MNSP co-precipitates are observed both in association with dislocations and apparently homogeneously distributed in the matrix. The MNSP appendage accounts for ≈ 95% (3.42%) of the total MNSP f ≈ 3.63%. The average A16 MNSP composition is similar to that in the low Cu steel A32, with an otherwise similar composition.

The f ≈ 3.42 and 3.83% in these medium Si and higher Mn A16 and A32 steels, decrease to ≈ 0.73% at very low 0.08 % Mn (A34), again mainly due to a lower N. The systematic effect of Mn “starvation” on limiting precipitation and modifying the phase selection was previously reported by Almirall et al. for the A-series steels NI to ≈ 0.2 dpa at 290°C [11]. Figure 11e shows that the CPI of a very low Mn, medium Si steel exhibits an enormous amount of Ni, and to a lesser extent Si, segregation to dislocations. In contrast, a limited amount of Mn is located in precipitates on the dislocations, mainly at their intersections.

Figure 11f shows an APT solute map for a low Cu and very low 0.2 at.% Ni alloy with medium 1.31 Mn and high 1.21 Si (A37). Table 6 shows a small MNSP f ≈ 0.58% in this case. All three solutes segregate to dislocations in A37, again forming precipitates at their intersections as well as along them, in string of pearls fashion. The MNSPs in the low Ni, high

Si steel contain almost equal amounts of Ni and Si, with compositions of ≈ $Ni_2Si_2Mn$. These compositions are in the vicinity of the Fe-Mn-Ni-Si quaternary MnSi phase field.

**Figure 11.**

Table 5. Bulk, matrix and precipitate Cu, Ni, Mn and Si compositions obtained from APT measurements for the very high fluence ion (DuET:H) and neutron irradiation (ATR-1) conditions.

| Alloy | Bulk Comp. (%) | | | | Matrix Comp. (%) | | | | Precipitate Comp. Fraction % | | | |
|---|---|---|---|---|---|---|---|---|---|---|---|---|
| | Cu | Ni | Mn | Si | Cu | Ni | Mn | Si | Cu | Ni | Mn | Si |
| LD:ATR-1 | 0.25 | 1.18 | 1.08 | 0.54 | 0.04 | 0.21 | 0.57 | 0.08 | 10.3 | 46.9 | 22.5 | 20.3 |
| LD:DuET:H | 0.23 | 1.22 | 1.12 | 0.54 | 0.10 | 0.29 | 1.24 | 0.17 | 8.5 | 50.2 | 20.9 | 20.4 |
| LG:ATR-1 | 0.00 | 0.71 | 0.87 | 0.43 | 0.00 | 0.11 | 0.38 | 0.10 | 0.2 | 46.1 | 31.2 | 22.5 |
| CM6:ATR-1 | 0.00 | 1.69 | 1.42 | 0.39 | 0.00 | 0.21 | 0.31 | 0.04 | 0.1 | 52.5 | 35.5 | 11.9 |
| A13:DuET:H | 0.05 | 3.23 | 0.98 | 1.26 | 0.02 | 0.53 | 0.39 | 0.16 | 0.5 | 60.9 | 13.9 | 24.7 |
| A16:DuET:H | 0.25 | 3.05 | 0.98 | 0.39 | 0.05 | 0.72 | 0.40 | 0.03 | 5.7 | 65.1 | 19.3 | 9.9 |
| A22:DuET:H | 0.05 | 1.82 | 1.28 | 0.51 | 0.03 | 0.46 | 0.75 | 0.10 | 0.9 | 57.5 | 23.9 | 17.7 |
| A28:DuET:H | 0.05 | 3.69 | 0.29 | 1.31 | 0.03 | 1.02 | 0.09 | 0.26 | 0.6 | 68.0 | 5.00 | 26.5 |
| A32:DuET:H | 0.04 | 3.10 | 1.26 | 0.45 | 0.01 | 0.62 | 0.43 | 0.03 | 0.6 | 65.9 | 22.7 | 10.8 |
| A34:DuET:H | 0.05 | 3.51 | 0.08 | 0.43 | 0.03 | 0.81 | 0.04 | 0.05 | 0.9 | 67.7 | 8.2 | 23.1 |
| A37:DuET:H | 0.04 | 0.19 | 1.31 | 1.21 | 0.04 | 0.04 | 1.21 | 0.73 | 1.4 | 38.4 | 20.4 | 39.8 |
| A39:DuET:H | 0.03 | 0.57 | 0.91 | 0.36 | 0.02 | 0.19 | 0.61 | 0.17 | 0.8 | 47.0 | 29.3 | 22.9 |

Table 6. Bulk Cu, Ni, Mn and Si compositions and APT precipitate <d>, N and f for the very high fluence ion (DuET:H) and neutron irradiation (ATR-1) conditions.

| Alloy | APT Bulk Comp (at.%) | | | | <d> | +/- | N | +/- | f | +/- | $10^6$ ions |
|---|---|---|---|---|---|---|---|---|---|---|---|
| | Cu | Ni | Mn | Si | (nm) | (nm) | ($10^{23}$ m$^{-3}$) | ($10^{23}$ m$^{-3}$) | (%) | (%) | |
| LD:ATR-1 | 0.25 | 1.18 | 1.08 | 0.54 | 4.01 | 0.31 | 6.98 | 1.26 | 2.11 | 0.23 | 40.8 |
| LD:DuET:H | 0.23 | 1.22 | 1.12 | 0.54 | 4.65 | 0.39 | 3.33 | 0.32 | 1.97 | 0.32 | 160.0 |
| LG:ATR-1 | 0.00 | 0.71 | 0.87 | 0.43 | 2.54 | 0.10 | 15.5 | 1.61 | 1.33 | 0.03 | 26.5 |
| CM6:ATR-1 | 0.00 | 1.69 | 1.42 | 0.39 | 3.18 | 0.09 | 17.3 | 1.32 | 2.82 | 0.14 | 30.0 |
| A13:DuET:H | 0.05 | 3.23 | 0.98 | 1.26 | 5.45 | 0.01 | 6.62 | 1.26 | 4.51 | 0.18 | 17.1 |
| A16:DuET:H | 0.25 | 3.05 | 0.98 | 0.39 | 5.82 | 1.07 | 2.22 | 1.44 | 3.63 | 0.24 | 77.0 |
| A22:DuET:H | 0.05 | 1.82 | 1.28 | 0.51 | 4.99 | 0.35 | 4.85 | 0.62 | 2.40 | 0.39 | 31.5 |
| A28:DuET:H | 0.05 | 3.69 | 0.29 | 1.31 | 4.75 | 0.79 | 5.90 | 1.81 | 3.95 | 0.08 | 19.2 |
| A32:DuET:H | 0.04 | 3.10 | 1.26 | 0.45 | 5.74 | 0.57 | 4.73 | 0.47 | 3.83 | 0.38 | 12.0 |
| A34:DuET:H | 0.05 | 3.51 | 0.08 | 0.43 | 5.32 | 0.53 | 1.08 | 0.11 | 0.73 | 0.07 | 21.2 |
| A37:DuET:H | 0.04 | 0.19 | 1.31 | 1.21 | 4.03 | 1.23 | 0.56 | 0.57 | 0.58 | 0.25 | 52.3 |
| A39:DuET:H | 0.03 | 0.57 | 0.91 | 0.36 | 4.05 | 0.30 | 3.26 | 0.13 | 0.91 | 0.40 | 14.9 |

Visual examination of all of the APT maps in Figure 11 shows major to massive amounts of solute segregation to dislocation segments. The role of solute segregated dislocations, and dislocation loops, acting as heterogeneous precipitate nucleation sites, is both widely observed and important [4,11,27,38,46,70]. Models for heterogeneous nucleation of precipitates in irradiated RPV steels have been proposed by both H. Ke et al. and Mamivand et al., based on CALPHAD thermodynamics [36] and RED kinetics [37,38]. JH. Ke et al. also developed a model for MNSP formation in under saturated Fe-9Cr steels, due to RIS at dislocations, even in alloys containing only small amounts of Mn, Ni and Si [46]. It is also visually evident in Figure 11 that the CPI A-series alloys have high to very high dislocation densities. A detailed discussion of dislocation structures and the character, as well as the causes and consequences of the corresponding solute segregation, is beyond the scope of this paper. However, these key topics are being addressed in detail as part of ongoing work.

To more fully illustrate the previous discussion, Figure 12a shows cross plots of the individual effects of variations in Cu, Mn, Ni and Si on <d>, N and f of the MNSPs. Note that Cu is not included in the MNSP f; the precipitate Cu is < 2 % with the exception of LD and A16 steels. The lines are simply to guide the eye. Except in the case of the Cu bearing steels, N and f increase with the solute content. The <d> does not vary much with Mn and Si, but increases slightly with Ni. At very high Ni ≈ 3.2 %, the f reaches very large values of more than 4%.

The stacked bar graphs in Figure 12b show the Mn, Si and Ni contents of both the steels and precipitates for all of the compositions in the high dpa CPI condition. As noted above, the f values are lowest for the steels with low Mn and Ni. For steels with more typical Mn contents, f increases systematically with Ni. Notably, the data shows that higher Si also increases f. A large effect of Si has not been observed in the case of NI at a lower ≈ 0.20 dpa and 320°C [11]. The solid lines show that the precipitate to alloy solute content ratio ($f/[X_{Ni}+X_{Mn}+X_{Si}]$)

increases with the steel Mn+Ni+Si. Finally, while the f is smaller for low Mn and Ni steels, it is not insignificant. The dominant effect of Ni is also shown in Figure 12c, plotting 2Ni + Cu versus the total f (including Cu) for both high dpa NI and CPI conditions. Ni dominance is due to the fact that Ni ≈ Mn + Si in both the G and $\Gamma_2$ phase type precipitates [11,31,36,37]. As shown in Figure 12c, the high dpa NI f fall ≈ 37% above those for CPI conditions; again, this is likely a result of the much higher CPI dpa rates.

**Figure 12.**

As noted previously, MNSPs are typically G and $\Gamma_2$ type phase compositions. However, these phases cannot form at very low Mn, Si and Ni. Thus the lower, but still significant, f in in these solute poor alloys suggests the selection of other phases. Figure 13 shows the Mn-Ni-Si projection of the Fe-Mn-Ni-Si quaternary at 277°C for the A-series steels in this study. Note, there is not a significant difference between the CALPHAD predictions at 277 and 290°C [37]. For typical RPV steel bulk Mn (≈ 0.8-1.5 %), Ni(≈ 0.5-1.6%) and Si (0.2-1.2%) contents, the precipitate compositions are clustered around the G and $\Gamma_2$ phases, as expected. However, the compositions of two other alloys with low Mn (A28, A34) are close to the $Ni_3Si$ γ' phase, slightly alloyed with Mn. However, the TEM FFT power spectra shown in Figure S1 of the supplemental information suggests that the MNSP structure is consistent with $Ni_2Si$. The MNSPs in the low Ni A37 steel are closer to the phase field labeled MnSi, which actually spans a thermodynamic composition range of ≈ 28 to 38 % Ni. The precipitate composition in the A16 and A32 alloys, with the lower Si, high Mn and the highest Ni, fall slightly closer to the $Ni_3Mn$ than to the G phase. This may represent nonstoichiometric enrichment of Ni in the G-phase; or alloying of a $Ni_3Mn$ phase with Si. Note, that even though A16 contains ≈ 0.25 % of bulk Cu, the MNSP composition only slightly deviates from the low Cu A32 steel with an otherwise similar composition. This reflects the separate MNSP appendage formation on CRPs (see Figure 8). All of these results are highly consistent with trends observed in high dpa NI.

A major conclusion is that even with insufficient amounts of any of the Mn, Ni or Si needed to form typical G or $\Gamma_2$ type phases, other precipitates still form at very high dpa, albeit at a lower f.

**Figure 13.**

### *3.3 Thermodynamic analysis and discussion*

The MNSP observed in typical RPV steels are the $Ni_3Mn_2Si$ (nominal) $\Gamma_2$ phase or the $Ni_{16}Mn_6Si_7$ (nominal) G-phase [36–39,46]. These phases are formed by the following reactions

$$16Ni(s) + 6Mn(s) + 7Si(s) \Leftrightarrow Ni_{16}Mn_6Si_7 \quad (1a)$$

or

$$3Ni(s) + 2Mn(s) + 1Si(s) \Leftrightarrow Ni_3Mn_2Si \quad (1b)$$

Here, the (s) indicates dissolved solutes. Taking the precipitate activities as 1, the MNSP solvus is given by

$$\{[X_{Ni}]^{16}[X_{Mn}]^{6}[X_{Si}]^{7}\}^{1/29} = K_G(T) \quad (2a)$$

or

$$\{[X_{Ni}]^{3}[X_{Mn}]^{2}[X_{Si}]\}^{1/6} = K_{\Gamma 2}(T) \quad (2b)$$

Here, the $\{[X_{Ni}]^{16}[X_{Mn}]^{6}[X_{Si}]^{7}\}^{1/29}$ and $\{[X_{Ni}]^{3}[X_{Mn}]^{2}[X_{Si}]\}^{1/6}$ are solute products ($SP_{G/\Gamma 2}$) for G and $\Gamma_2$ phases, the $X_i$ are the dissolved solute mole fractions and $K_{G/\Gamma 2}(T)$ are the temperature dependent equilibrium reaction constant, that incorporates the activity coefficients of the dissolved solutes and the formation free energy of the pertinent G or $\Gamma_2$ phase. Ke used CALPHAD to determine the $K_{G/\Gamma 2}(T)$ for a range of typical RPV steel compositions as $K_G(290) \approx 2.56x10^{-3}$ and $K_{\Gamma 2}(290) \approx 2.21x10^{-3}$ [37,38].

The high dpa ATR-1 NI and DuET:H CPI both produce MNSP full precipitation. The limiting f, ignoring the Gibbs-Thomson effect, can be calculated as:

$$f_G \approx \{[X_{Ni} - (K_G/[X_{Mn}{}^{6}X_{Si}{}^{7}])^{(1/29)}\}/0.55 \quad (3a)$$

$$f_{\Gamma 2} \approx \{X_{Ni} - (K_{\Gamma}/[X_{Mn}{}^{2}X_{Si}])^{(1/6)}]/0.50 \quad (3b)$$

These estimates involve several assumptions. First they are for stoichiometric G and $\Gamma_2$ phases. Second Equations 3a and b assume that the alloy Ni content controls f. The third assumption is there is sufficient Mn and Ni to match the G phase or $\Gamma_2$ phase stoichiometric compositions. In reality, even in phases that are stoichiometric at full equilibrium, ranges of compositions are thermodynamically accessible if there are free energy reductions upon solute precipitation from solid solutions, as is the case prior to equilibrium. Further, higher chemical potentials of the individual solutes can alter the MNSP compositions so as to track the overall alloy chemistry. It has also been shown that Mn and Si trade off in MNSPs, again in response to the steel composition [11,31]. Finally, the nanoscale precipitate compositions are modified their interface energies that also depend on composition. These thermodynamic effects affecting MNSP compositions can be further modified by differences in the solute transport mechanisms and kinetics as a result of RIS.

More detailed thermokinetic models have been reported [37,38] and reduced order fully physical models will be the topic of future publications. Here we simply, assess how well the MNSP f correlates with the SPs at high dpa. Least square linear fits of f correlate slightly better with $SP_G$ than with $SP_{\Gamma2}$. Figure 14 plots the $SP_G$ fit to the CPI f data shown as green squares. The ATR-1 NI data are also shown as blue triangles. Notably, the high dpa CPI and NI $f(SP_G)$ follow very similar trends. They extrapolate to $f \approx 0$ at $SP_G \approx 0.002$, which is consistent with the calculated CALPHAD $K_G$(290°C). Since the bulk $SP_G$ does not account for the Gibbs-Thomson effect the actual $SP_G$ is actually may be slightly lower than the CALPHAD prediction. The red circles are lower dose ATR-2 NI to ≈ 0.2 dpa at 320°C. In this case, the f values are lower, as expected, indicating the effects of nucleation and initial growth at $SP_G$ less than about 0.01. However, for higher $SP_G$ the f trend is very similar that at high dpa.

**Figure 14.**

Figure 15 plots the f predicted by Equations 3a versus the measured values for CPI that result in G (or $\Gamma_2$) phase. The red circles are for alloys that have sufficient Mn and Si to form stoichiometric G phase, while the blue squares do not. In the case of alloys with sufficient Mn and Si to form G-phase, the best-fit line forced though 0 has a slope of 0.90, consistent with a small Gibbs-Thomson effect. The actual best-fit line has an f intercept of ≈ 0.004 and a slope of 0.71, consistent with a larger Gibbs-Thomson effect. As expected the high Ni data with insufficient Mn and Si to form stoichiometric G-phase fall below the extrapolated fit lines. Overall, the agreement between the predicted and measured f is surprisingly good and highly supportive of the thermodynamic analysis.

**Figure 15.**

### 3.4 Estimates of $\Delta\sigma_y$ and $\Delta T$

The APT f measured in the CPI can be used to estimate the corresponding irradiation hardening ($\Delta\sigma_y$) based on well-established dispersed barrier models [4,6,10,31,33,71,72]. However we use a simpler method using the empirical relation derived in [11].

$$\Delta\sigma_y \approx 314\sqrt{f(\%)}. \qquad (4)$$

The $\Delta\sigma_y$ for these alloys has been measured for the ATR-2 NI to a lower ≈ 0.20 dpa at 290°C. Thus, in order to compare predicted and measured $\Delta\sigma_y$, the CPI APT f must first be adjusted to ATR-2 NI condition, $f_{A2}$. Based on the trend in a number of other alloys irradiated in both ATR-1 (A1) and ATR-2 (A2), an empirical adjustment factor was found to be

$$f_{A2}/f_{A1} \approx 0.245Ni + 0.65Cu$$

Here Ni and Cu are the bulk alloy compositions. The $\Delta\sigma_y$ predicted $f_{A2}$ based on assuming the CPI $f_{cpi} \approx f_{A1}$ is plotted against the measured ATR-2 hardening in Figure 16a. The filled red symbols are for the alloys that form precipitates with G and $\Gamma_2$ type compositions. The filled blue squares are for high Ni, low to very low Mn steels that form $Ni_{2\text{-}3}Si$ type precipitate compositions. The lines are least square fits forced through 0,0. It appears that the $Ni_{2\text{-}3}Si$ type precipitates are weaker dislocation obstacles than those with G or $\Gamma_2$ phase type compositions. For perspective the estimated $\Delta T \approx 0.7\Delta\sigma_y$ is plotted in Figure 16b [72]. In alloys with high Ni and Mn the $\Delta T$ are large even at lower service relevant dpa.

**Figure 16.**

## 4. Conclusions

The results of this study, comparing NI and CPI, can be summarized as follows. The precipitate compositions are similar in both irradiation conditions. At high dpa MNSPs and CRP-MNSPs form in low Cu and Cu bearing alloys, respectively. In the latter case, lower dpa Cu core Mn-Ni-Si shell structures evolve into CRP-MNSP appendage co-precipitate features at high dpa. For a wide range of typical RPV steel compositions, the MNSPs have G and $\Gamma_2$ type phase compositions. CPI produces fewer and larger precipitates. Further, higher dpa are needed to form the same precipitate f for CPI versus NI conditions. The delayed precipitation is consistent with enhanced recombination of vacancies and SIA defects at higher CPI dpa rates, which reduces the efficiency of RED (and RIS). The MNSP grow slowly, but eventually reach large f at high dpa. Notably, f correlates well with the G-phase solute product, $(\mathrm{Ni}^{16}\mathrm{Mn}^{6}\mathrm{Si}^{7})^{(1/29)}$, and is close to the equilibrium value, slightly modified by the Gibbs-Thomson effect. However, in steels with very low Mn and high Ni and Si, $Ni_{2\text{-}3}Si$ silicide type compositions are selected rather than those for the G or $\Gamma_2$ type phases; and when Ni is low, a MnSi phase field type composition, which still contains ≈ 28-38% Ni, is observed. High Ni and Mn alloys with lower Si form $Ni_3Mn$ type precipitates alloyed with small amounts of Si (10-12%).

Thermodynamic models are able to predict the f for alloys with G and $\Gamma_2$ type precipitate compositions. Deviations are likely associated with the Gibbs-Thomson effect and/or insufficient Mn and Si to form precipitates with close to stoichiometric compositions. In this case Ni does not fully control f. The f from the CPI can be used to estimate $\Delta\sigma_y$ and $\Delta T$ at lower service relevant dpa. While not quantitatively accurate, this allows scoping studies of the embrittlement sensitivity of new RPV alloys. The $\Delta\sigma_y$ also suggest that Ni-Si dominated precipitates may be weaker dislocation obstacles than the G and $\Gamma_2$ type MNSPs.

## Data Availability

The raw/processed data required to reproduce these findings cannot be shared at this time due to technical or time limitations.

## References

[1] Climate Change and Nuclear Power 2018, International Atomic Energy Agency. Vienna (2018).

[2] J.T. Busby, Light Water Reactor Sustainability Materials Aging and Degradation Pathway Technical Program Plan ORNL/LTR-2012/327, (2012).

[3] Expanded Materials Degradation Assessment (EDMA): Aging of Reactor Pressure Vessels NUREG/CR-7153 V3, (2013).

[4] G.R. Odette, T. Yamamoto, T.J. Williams, R.K. Nanstad, C.A. English, On the history and status of reactor pressure vessel steel ductile to brittle transition temperature shift prediction models, J. Nucl. Mater. 526 (2019) 151863. doi:10.1016/j.jnucmat.2019.151863.

[5] G.R. Odette, B.D. Wirth, D.J. Bacon, N.M. Ghoniem, Multiscale-Multiphysics Modeling of Materials : Embrittlement of Pressure-Vessel Steels, MRS Bull. 26 (2001) 176–181. doi:10.1557/mrs2001.39.

[6] G.R. Odette, Neutron Irradiation Effects in Reactor Pressure Vessel Steels and Weldments, International Atomic Energy Agency, Vienna, IAEA IWG-LMNPP-98/3, 1998, p. 438. https://inis.iaea.org/collection/NCLCollectionStore/_Public/30/013/30013700.pdf.

[7] E.D. Eason, G.R. Odette, R.K. Nanstad, T. Yamamoto, A physically-based correlation of irradiation-induced transition temperature shifts for RPV steels, J. Nucl. Mater. 433 (2013) 240–254. doi:10.1016/j.jnucmat.2012.09.012.

[8] ASTM Subcommittee E10.02, Adjunct for ASTM E900-15: Technical Basis for the Equation used to Predict Radiation-Induced Transition Temperature shift in Reactor Vessel Materials, ASTM International, West Conshohocken, PA, 2015.

[9] G.R. Odette, R.K. Nanstad, Predictive reactor pressure vessel steel irradiation embrittlement models: Issues and opportunities, JOM. 61 (2009) 17–23. doi:10.1007/s11837-009-0097-4.

[10] G.R. Odette, G.E. Lucas, Recent progress in understanding reactor pressure vessel steel embrittlement, Radiat. Eff. Defects Solids. 144 (1998) 189–231. doi:10.1080/10420159808229676.

[11] N. Almirall, P.B. Wells, T. Yamamoto, K. Wilford, T. Williams, N. Riddle, G.R. Odette, Precipitation and Hardening in Irradiated Low Alloy Steels with a Wide Range of Ni and Mn Compositions, Acta Mater. 179 (2019) 119–128. doi:10.1016/j.actamat.2019.08.027.

[12] M.G. Burke, R.J. Stofanak, J.M. Hyde, C.A. English, W.L. Server, Microstructural aspects of irradiation damage in A508 Gr 4N forging steel: Composition and flux effects, J. ASTM Int. 1 (2002) 1–14. doi:10.1520/JAI11773.

[13] G. Wire, W. Beggs, T. Leax, Evaluation of irradiation embrittlement of A508 Gr 4N and comparison to other low-alloy steels, in: 21st Int. Symp. Eff. Radiat. Mater., 2002: pp. 179–193. doi:10.1520/STP11227S.

[14] T. Leax, Temperature dependence and variability of fracture toughness in the transition regime for A508 grade 4N pressure vessel steel, 5th Int. ASTM/ESIS Symp. Fatigue Fract. 3 (2005) 1–20. doi:10.1520/JAI13230.

[15] M. Kim, S. Park, B. Lee, K. Lee, Comparison of Fracture Properties in SA508 Gr.3, Gr.4N high strength low alloy steels for advanced pressure vessel materials, Int. J. Press. Vessel. Pip. 131 (2015) 60–66. doi:10.1016/j.ijpvp.2015.04.010.

[16] S. Wu, H. Jin, Y. Sun, E. Al., Critical cleavage fracture stress characterization of A508 nuclear pressure vessel steels, Int. J. Press. Vessel. Pip. 123 (2014) 92–98. doi:10.1016/j.ijpvp.2014.08.003.

[17] G.R. Odette, On the dominant mechanism of irradiation embrittlement of reactor pressure vessel steels, Scr. Metall. 17 (1983) 1183–1188. doi:10.1016/0036-9748(83)90280-6.

[18] G.R. Odette, Radiation induced microstructural evolution in reactor pressure vessel steels, in: Mater. Res. Soc. Symp. - Proc., Materials Research Society, 1995: pp. 137–148. doi:10.1557/PROC-373-137.

[19] G. R. Odette, "On the Composition and Structure of Nanoprecipitates in Irradiated Pressure Vessel Steels", Microstructure Evolution During Irradiation, Mat. Res. Soc. Symp. Proc. 439 (1996) 457-468.

[20] G.R. Odette, B.D. Wirth, A computational microscopy study of nanostructural evolution in irradiated pressure vessel steels, J. Nucl. Mater. 251 (1997) 157–171. doi:10.1016/S0022-3115(97)00267-5.

[21] C.L. Liu, G.R. Odette, B.D. Wirth, G.E. Lucas, A lattice Monte Carlo simulation of nanophase compositions and structures in irradiated pressure vessel Fe-Cu-Ni-Mn-Si steels, Mater. Sci. Eng. A. 238 (1997) 202–209. doi:10.1016/S0921-5093(97)00450-4.

[22] G.R. Odette, G.E. Lucas, The Effect of Heat Treatment on Irradiation Hardening of Pressure Vessel Steels: Data Trends and Mechanisms, in: Proceddings of the 2nd International Symposium on Environmental Degradation of Materials for Nuclear Power Sustems-Water Reactors, ANS. (1986) 295.

[23] P.N. Randall, Basis for Revision 2 of the US Regulatory Commission's Regulatory Guide 1.99, Radiation Embrittlement of Nuclear Reactor Pressure Vessels an International Review (Second Volume), ASTM STP 909-2, ASTM (1986) pp. 149–162.

[24] U.S. Nuclear Regulatory Commission, Radiation Embrittlement of Reactor Vessel Materials, Regulatory Guide 1.99 Rev. 2, 1988.

[25] G.R. Odette, T. Yamamoto, B.D. Wirth, Late Blooming phases and Dose Rate Effects in RPV Steels: Integrated Experiments and Models, Proceeding of the Second International Conference on Multiscale Modeling, October 11-15, 2004, Los Angeles, CA (2004) pp. 10.

[26] M.K. Miller, M.A. Sokolov, R.K. Nanstad, K.F. Russell, APT characterization of high nickel RPV steels, J. Nucl. Mater. 351 (2006) 187–196. doi:10.1016/j.jnucmat.2006.02.013.

[27] N. Almirall, P.B. Wells, H. Ke, P. Edmondson, D. Morgan, T. Yamamoto, G.R. Odette, On the elevated temperature thermal stability of nanoscale Mn-Ni-Si precipitates formed at lower temperature in highly irradiated reactor pressure vessel steels, Sci. Rep. 9 (2019). doi:10.1038/s41598-019-45944-z.

[28] M.K. Miller, K.F. Russell, Embrittlement of RPV steels: An atom probe tomography perspective, J. Nucl. Mater. 371 (2007) 145–160. doi:10.1016/j.jnucmat.2007.05.003.

[29] T. Takeuchi, A. Kuramoto, J. Kameda, T. Toyama, Y. Nagai, M. Hasegawa, T. Ohkubo, T. Yoshiie, Y. Nishiyama, K. Onizawa, Effects of chemical composition and dose on microstructure evolution and hardening of neutron-irradiated reactor pressure vessel steels, J. Nucl. Mater. 402 (2010) 93–101. doi:10.1016/j.jnucmat.2010.04.008.

[30] J.M. Hyde, M.G. Burke, B. Gault, D.W. Saxey, P. Styman, K.B. Wilford, T.J. Williams, Atom probe tomography of reactor pressure vessel steels: an analysis of data integrity., Ultramicroscopy. 111 (2011) 676–82. doi:10.1016/j.ultramic.2010.12.033.

[31] P.B. Wells, T. Yamamoto, B. Miller, T. Milot, J. Cole, Y. Wu, G.R. Odette, Evolution of manganese–nickel–silicon-dominated phases in highly irradiated reactor pressure vessel steels, Acta Mater. 80 (2014) 205–219. doi:10.1016/j.actamat.2014.07.040.

[32] P.D. Styman, J.M. Hyde, D. Parfitt, K. Wilford, M.G. Burke, C. a. English, P. Efsing, Post-irradiation annealing of Ni–Mn–Si-enriched clusters in a neutron-irradiated RPV steel weld using Atom Probe Tomography, J. Nucl. Mater. 459 (2015) 127–134. doi:10.1016/j.jnucmat.2015.01.027.

[33] P.B. Wells, The Character and Stability of Mn-Ni-Si Precipitates in Reactor Pressure Vessel Steels [PhD Thesis], Univ. Calif. St. Barbar. (2015).

[34] P.D. Edmondson, M.K. Miller, K.A. Powers, R.K. Nanstad, Atom probe tomography characterization of neutron irradiated surveillance samples from the R . E . Ginna reactor pressure vessel, J. Nucl. Mater. 470 (2016) 147–154. doi:10.1016/j.jnucmat.2015.12.038.

[35] D.J. Sprouster, J. Sinsheimer, E. Dooryhee, S.K. Ghose, P. Wells, T. Stan, N. Almirall, G.R. Odette, L.E. Ecker, Structural characterization of nanoscale intermetallic precipitates in highly neutron irradiated reactor pressure vessel steels, Scr. Mater. 113 (2016) 18–22. doi:10.1016/j.scriptamat.2015.10.019.

[36] W. Xiong, H. Ke, P.B. Wells, L. Barnard, R. Krishnamurthy, G.R. Odette, D. Morgan, Thermodynamic models of low temperature Mn-Ni-Si precipitation in reactor pressure vessel steels, Mater. Res. Soc. Commun. 4 (2014) 101–105. doi:10.1557/mrc.2014.21.

[37] H. Ke, P. Wells, P.D. Edmondson, N. Almirall, L. Barnard, G.R. Odette, D. Morgan, Thermodynamic and kinetic modeling of Mn-Ni-Si precipitates in low-Cu reactor pressure vessel steels, Acta Mater. 138 (2017) 10–26. doi:10.1016/j.actamat.2017.07.021.

[38] M. Mamivand, P. Wells, H. Ke, S. Shu, G. R. Odette, D. Morgan, CuMnNiSi precipitate evolution in irradiated reactor pressure vessel steels: integrated cluster dynamics and experiments, Acta Materialia (2019) in press.

[39] S. Shu, P.B. Wells, N. Almirall, G.R. Odette, D.D. Morgan, Thermodynamics and kinetics of core-shell versus appendage co-precipitation morphologies: An example in the Fe-Cu-Mn-Ni-Si system, Acta Mater. 157 (2018) 298–306. doi:10.1016/j.actamat.2018.07.037.

[40] G.R. Odette, C.L. Liu, B.D. Wirth, On the Composition and Structure of Nanoprecipitates in Irradiated Pressure Vessel Steels, Mater. Res. Soc. Symp. Proc. 439 (1997) 457–469. doi:10.1557/PROC-439-457.

[41] G.S. Was, Fundamentals of Radiation Materials Science, Springer, 2007.

[42] G. Was, Challenges to the use of ion irradiation for emulating reactor irradiation, J. Mater. Res. 30 (2015) 1158–1182. doi:10.1557/jmr.2015.73.

[43] B. Heidrich, S.M. Pimblott, G.S. Was, S. Zinkle, Roadmap for the application of ion beam technologies to the challenges of nuclear energy technologies, Nucl. Instruments Methods Phys. Res. Sect. B Beam Interact. with Mater. Atoms. 441 (2019) 41–45. doi:10.1016/J.NIMB.2018.12.022.

[44] G.S. Was, M. Hash, G.R. Odette, Hardening and microstructure evolution in proton-irradiated model and commercial pressure-vessel steels, Phi. 85 (2005) 703–722. doi:10.1080/14786430412331319974.

[45] S. Shu, N. Almirall, P.B. Wells, T. Yamamoto, G.R. Odette, D.D. Morgan, Precipitation in Fe-Cu and Fe-Cu-Mn model alloys under irradiation: Dose rate effects, Acta Mater. 157 (2018) 72–82. doi:10.1016/j.actamat.2018.07.017.

[46] J.H. Ke, H. Ke, G.R. Odette, D. Morgan, Cluster dynamics modeling of Mn-Ni-Si precipitates in ferritic-martensitic steel under irradiation, J. Nucl. Mater. 498 (2018) 83–88. doi:10.1016/j.jnucmat.2017.10.008.

[47] J.H. Ke, E.R. Reese, E.A. Marquis, G.R. Odette, D. Morgan, Flux effects in precipitation under irradiation – Simulation of Fe-Cr alloys, Acta Mater. 164 (2019) 586–601. doi:10.1016/J.ACTAMAT.2018.10.063.

[48] A.M. Monterrosa, D. Woodley, Z.J. Jiao, G. Was, The influence of carbon on cavity evolution in ion-irradiated ferritic-martensitic steels, J. Nucl. Mater. 509 (2019) 722-735.

[49] M.P. Short, D.R. Gaston, M. Jin, L. Shao, F.A. Garner, Modeling injected interstitial effects on void swelling in self-ion irradiation experiments, J. Nucl. Mater. 471 (2016) 200–207. doi:10.1016/j.jnucmat.2015.10.002.

[50] Malerba, L. (2008). Personal Communication.

[51] J.W. Nielsen, As-Run Physics Analysis for the UCSB-1 Experiment in the Advanced Test Reactor, 2015.

[52] ECAR-2982, As-Run Thermal Analysis for the UCSB-1 Experiment in the Advanced Test Reactor, S.M. Wilson, November 2015., n.d.

[53] ASTM E521, Standard Practice for Neutron Radiation Damage Simulation by ChargedParticle Irradiation, Annual Book of ASTM Standards, Vol. 12.02, ASTM International, West Conshohocken, PA.

[54] W.R. McKenzie, E.A. Marquis, P.R. Munroe, Focused Ion Beam Sample Preparation for Atom Probe Tomography, Microsc. Sci. Technol. Appl. Educ. 3 (2010) 1800–1810. http://www.formatex.info/microscopy4/1800-1810.pdf.

[55] K. Thompson, D. Lawrence, D.J. Larson, J.D. Olson, T.F. Kelly, B. Gorman, In situ site-specific specimen preparation for atom probe tomography, Ultramicroscopy. 107 (2007) 131–139. doi:10.1016/j.ultramic.2006.06.008.

[56] M.K. Miller, Atom Probe Tomography, Kluwer Academic/Plenum Publishers, 2000.

[57] B. Gault ; M.P. Moody; J.M. Cairney; S.P. Ringer, Atom Probe Microscopy, Springer, 2012.

[58] E.A. Marquis, J.M. Hyde, Applications of atom-probe tomography to the characterisation of solute behaviours, Mater. Sci. Eng. R Reports. 69 (2010) 37–62. doi:10.1016/j.mser.2010.05.001.

[59] J.M. Hyde, A. Cerezo, R.P. Setna, P.J. Warren, G.D.W. Smith, Lateral and depth scale calibration of the position sensitive atom probe, Appl. Surf. Sci. 76–77 (1994) 382–391. doi:10.1016/0169-4332(94)90371-9.

[60] J.M. Hyde, E.A. Marquis, K.B. Wilford, T.J. Williams, A sensitivity analysis of the maximum separation method for the characterisation of solute clusters, Ultramicroscopy. 111 (2011) 440–447. doi:10.1016/j.ultramic.2010.12.015.

[61] C. A. Williams, D. Haley, E.A. Marquis, G.D.W. Smith, M.P. Moody, Defining clusters in APT reconstructions of ODS steels., Ultramicroscopy. 132 (2013) 271–8. doi:10.1016/j.ultramic.2012.12.011.

[62] D.J. Larson, B. Gault, B.P. Geiser, F. De Geuser, F. Vurpillot, Atom probe tomography spatial reconstruction: Status and directions, Curr. Opin. Solid State Mater. Sci. 17 (2013) 236–247. doi:10.1016/j.cossms.2013.09.002.

[63] B. Gault, F. De Geuser, L.T. Stephenson, M.P. Moody, B.C. Muddle, S.P. Ringer, Microscopy Microanalysis Estimation of the Reconstruction Parameters for Atom Probe Tomography, Microsc. Microanal. 14 (2008) 296–305. doi:10.1017/S1431927608080690.

[64] P.D. Edmondson, C.M. Parish, R.K. Nanstad, Using complimentary microscopy methods to examine Ni-Mn-Si-precipitates in highly-irradiated reactor pressure vessel steels, Acta Mater. 134 (2017) 31–39. doi:10.1016/j.actamat.2017.05.043.

[65] J.M. Hyde, M.G. Burke, G.D.W. Smith, P. Styman, H. Swan, K. Wilford, Uncertainties and assumptions associated with APT and SANS characterisation of irradiation damage in RPV steels, J. Nucl. Mater. 449 (2014) 308–314. doi:10.1016/j.jnucmat.2013.07.029.

[66] N.J. Cunningham, Study of the Structure, Composition, and Stability of Y-Ti-O nm-Scale Features in Nano-Structured Ferritic Alloys [PhD Thesis], Univ. Calif. St. Barbar. (2012).

[67] E.A. Marquis, F. Vurpillot, Chromatic aberrations in the field evaporation behavior of small precipitates, Microsc. Microanal. 14 (2008) 561–570. doi:10.1017/S1431927608080793.

[68] C. Hatzoglou, B. Radiguet, P. Pareige, Experimental artefacts occurring during atom probe tomography analysis of oxide nanoparticles in metallic matrix: Quantification and correction, J. Nucl. Mater. 492 (2017) 279–291. doi:10.1016/j.jnucmat.2017.05.008.

[69] E.A. Marquis, Atom probe tomography applied to the analysis of irradiated microstructures, J. Mater. Res. 30 (2015) 1–9. doi:10.1557/jmr.2014.398.

[70] H. Ke, P. Wells, P.D. Edmondson, N. Almirall, L. Barnard, G.R. Odette, D. Morgan, Thermodynamic and kinetic modeling of Mn-Ni-Si precipitates in low-Cu reactor pressure vessel steels, Acta Mater. 138 (2017) 10–26. doi:10.1016/j.actamat.2017.07.021.

[71] D. Bhattacharyya, T. Yamamoto, P. Wells, E. Marquis, M. Bachhav, Y. Wu, J. Davis, A. Xu, G.R. Odette, Microstructural changes and their effect on hardening in neutron irradiated Fe-Cr alloys, J. Nucl. Mater. (2019).

[72] E.D. Eason, G.R. Odette, R.K. Nanstad, T. Yamamoto, A physically based correlation of irradiation-induced transition temperature shifts for RPV steels Ch2., Oak Ridge National Lab, 2007. https://info.ornl.gov/sites/publications/files/Pub2592.pdf.

## Acknowledgements

The authors gratefully acknowledge funding the U.S. Department of Energy (DOE) via a Light Water Reactor Sustainability (LWRS) program subcontract from Oak Ridge National Laboratory (ORNL). The advanced steel series used in this work were provided by Rolls Royce (RR); and the design and acquisition of the alloy matrix was due the efforts of RR researchers Dr. Keith Wilford and Tim Williams. The Nuclear Science User Facilities (NSUF) program, at the Idaho National Laboratory (INL), sponsored the UCSB ATR-1 irradiation. The NSUF also funded FIB and APT LEAP access at the DOE sponsored Center for Advanced Energy Studies (CAES) in Idaho Falls, as well as a DOE Nuclear University Program fellowship. The CPI was carried out at the Dual Beam Facility for Energy Science and Technology (DuET) at Kyoto University in Japan with the support of Mr. O. Hashitomi. All the APT studies were conducted at the CAES facility, or the UCSB California Nano Science Institute (CNSI), which is supported by the National Science Foundation. The authors express gratitude for the assistance given by the support staff at CAES and CNSI. We also thank Drs. Randy Nanstad, Janet Robertson and Keith Leonard at ORNL for their advice, encouragement and technical support. We are also grateful for insights provided by our modeling collaboration with Professor Dane Morgan's group at the University of Wisconsin, and especially the work of Drs. Huibin Ke and Mahmood Mamivand. In particular, we note the helpful advice Dr. Ke provided regarding the solute products used in the simplified thermodynamic modeling section.  Finally, this work was made possible by our UCSB colleagues David Gragg and Kirk Fields, though their central and critical role in all aspects of the irradiation experiment and post irradiation mechanical testing.

# Figures

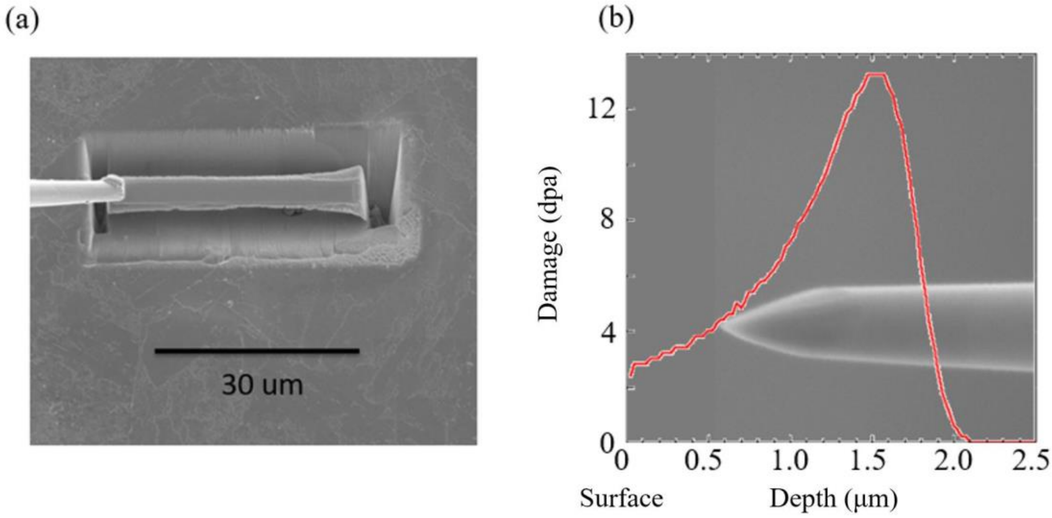

Figure 1. a) A scanning electron microscope image showing the FIB liftout from a CPI steel that is subsequently sectioned and mounted onto the micro-tip posts; and, b) annular milling produces a FIB sharpened APT specimen with the SRIM calculated damage (peak of 13 dpa) as a function of depth overlaid.

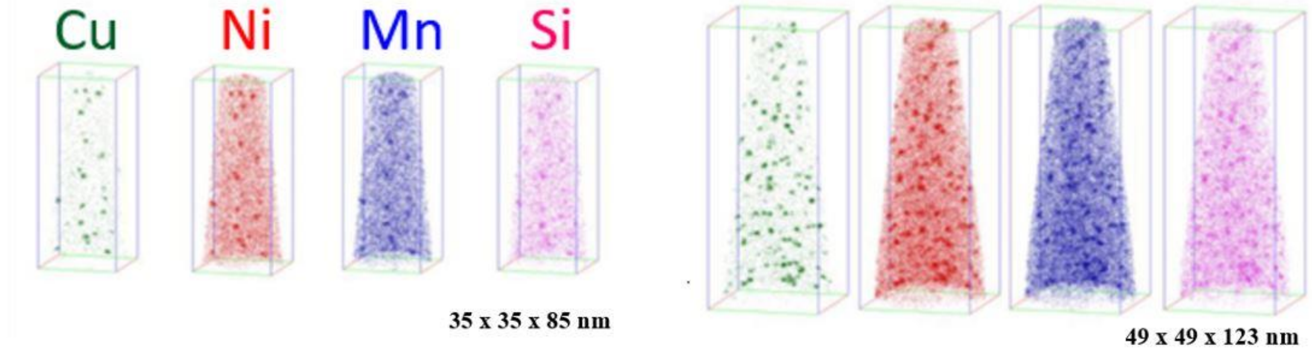

(a) LI Neutron Irradiated 0.15% Cu 0.71% Ni (at.%)

(c) LD Neutron Irradiated 0.24% Cu 1.03% Ni (at.%)

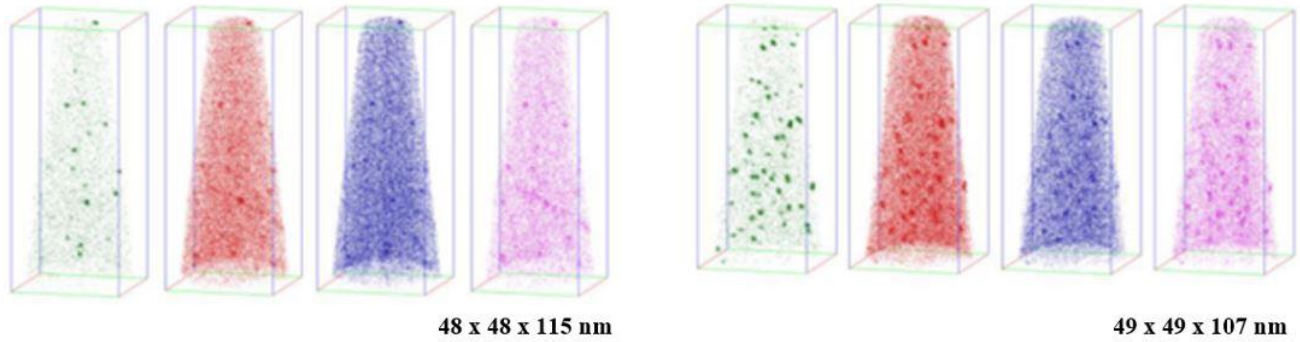

(b) LI Ion Irradiated 0.15% Cu 0.71% Ni (at.%)

(d) LD Ion Irradiated 0.24% Cu 1.03% Ni (at.%)

Figure 2. Solute maps directly comparing lower dpa ≈ 0.2 dpa CPI (DuET:L) and NI (BR2) conditions at nominally a-b) medium 0.15% Cu and 0.71% Ni (LI); and, c-d) high 0.24% Cu and 1.03% Ni (LD). All compositions are in at.%.

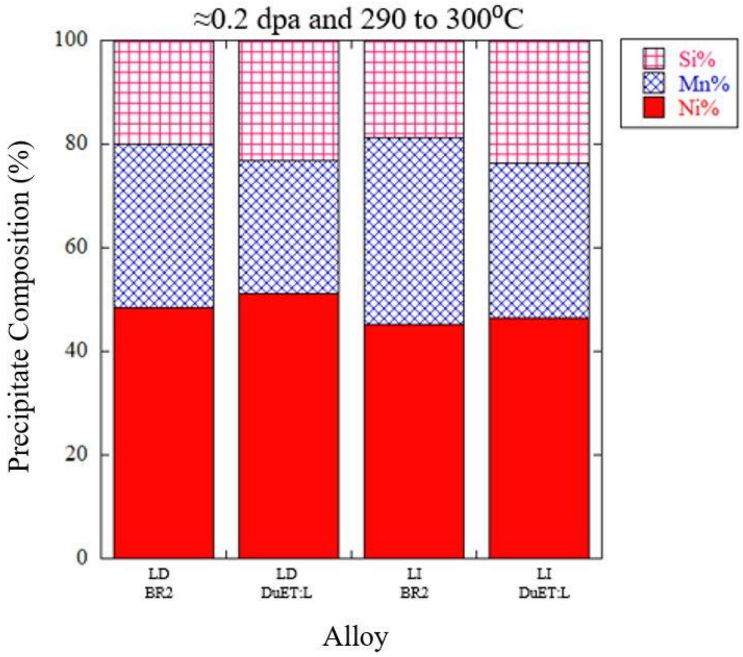

Figure 3. Bar graphs comparing the Ni, Mn, and Si precipitate compositions for the lower dpa NI (BR2) and CPI (DuET:L) high 1.03% Ni (LD) and medium 0.71% Ni (LI) steels. All compositions are in at.%.

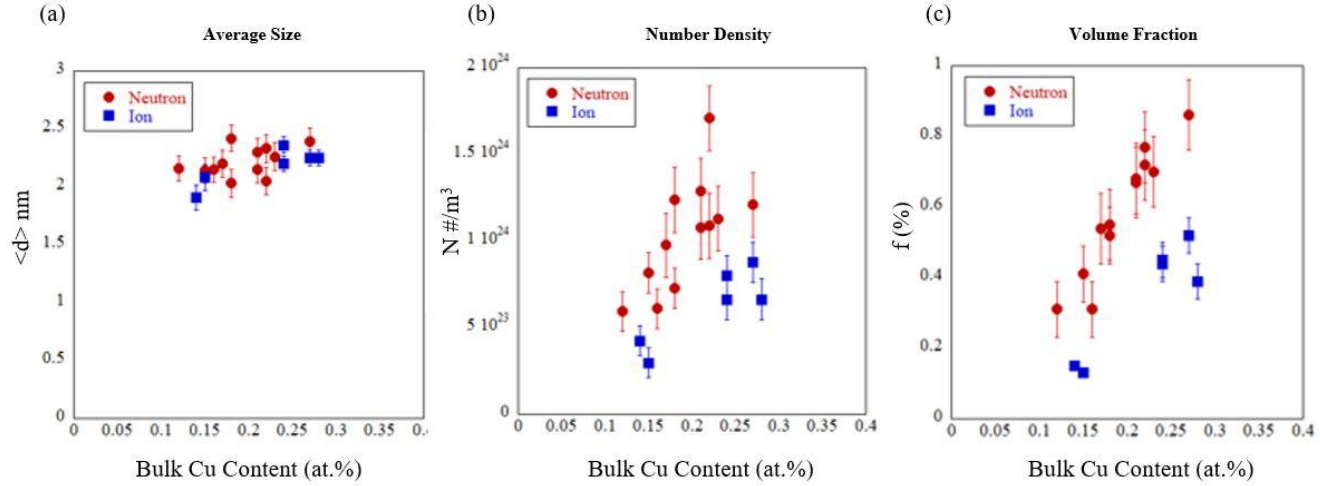

Figure 4. The lower dpa CPI (DuET:L) and NI (BR2) individual tip bulk Cu content dependence of the precipitate: a) <d>; b) N; and, c) f. Note the higher Cu alloy also contains higher Ni.

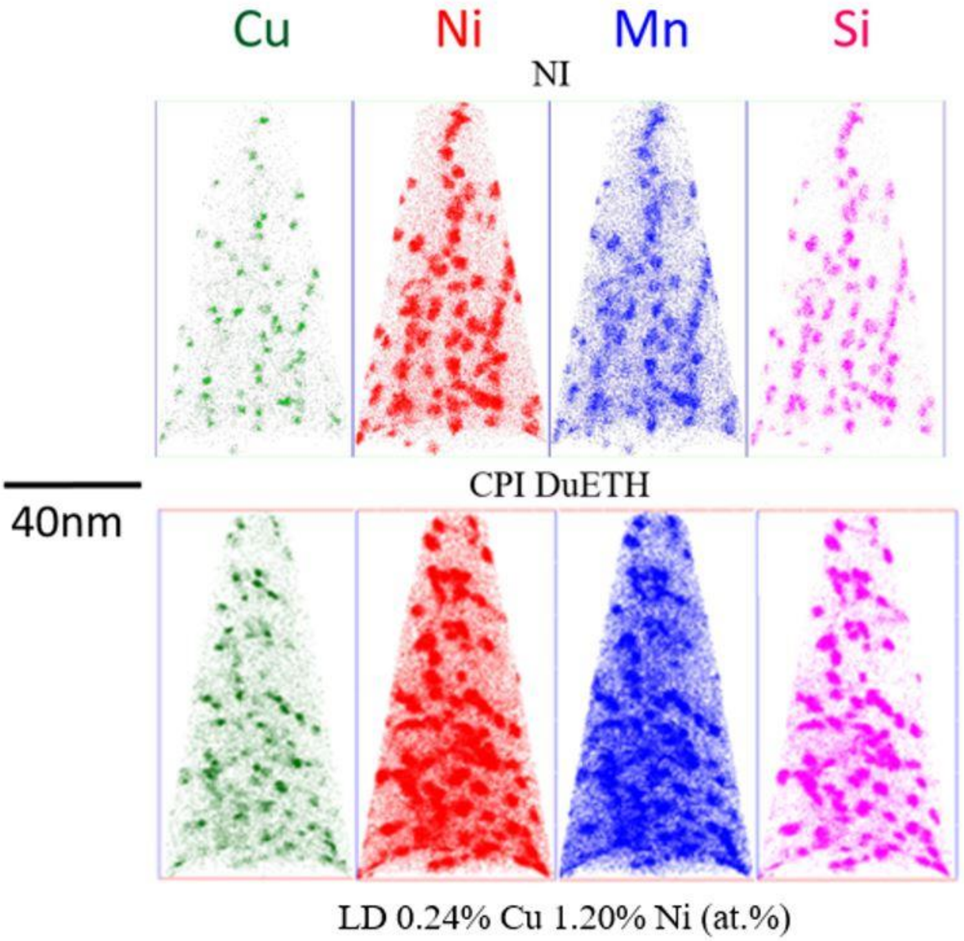

Figure 5. Solute maps directly comparing the high dpa ATR1 NI and DuET:H CPI for nominally the 1.20% Ni and 0.24% Cu steel (LD). This steel also contains 1.08 to 1.12% Mn and 0.54% Si. All compositions are in at.%.

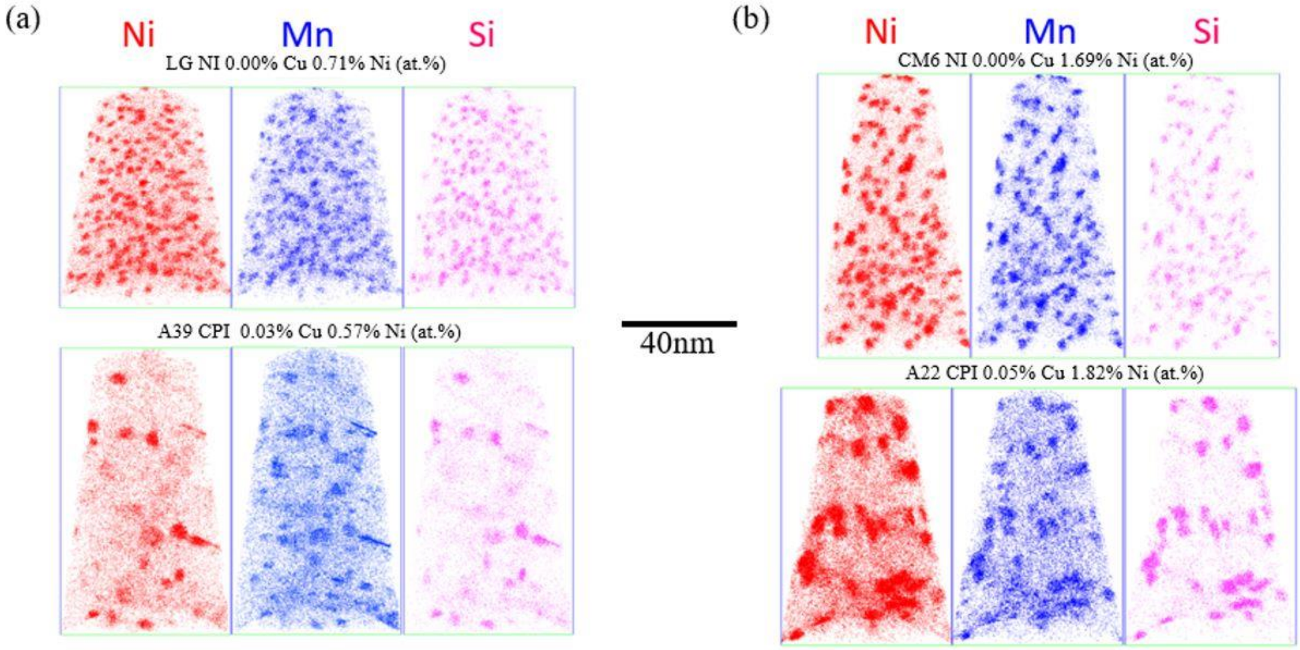

Figure 6. Solute maps for DuET:H CPI and ATR1 NI conditions, comparing compositionally similar low ≈ 0.05% Cu steels: a) LG/A39 (0.71 and 0.57% Ni) and b) CM6/A22 (1.69 and 1.82% Ni). These steels contain 0.87-1.42% Mn and 0.36-0.51% Si. All compositions are in at.%.

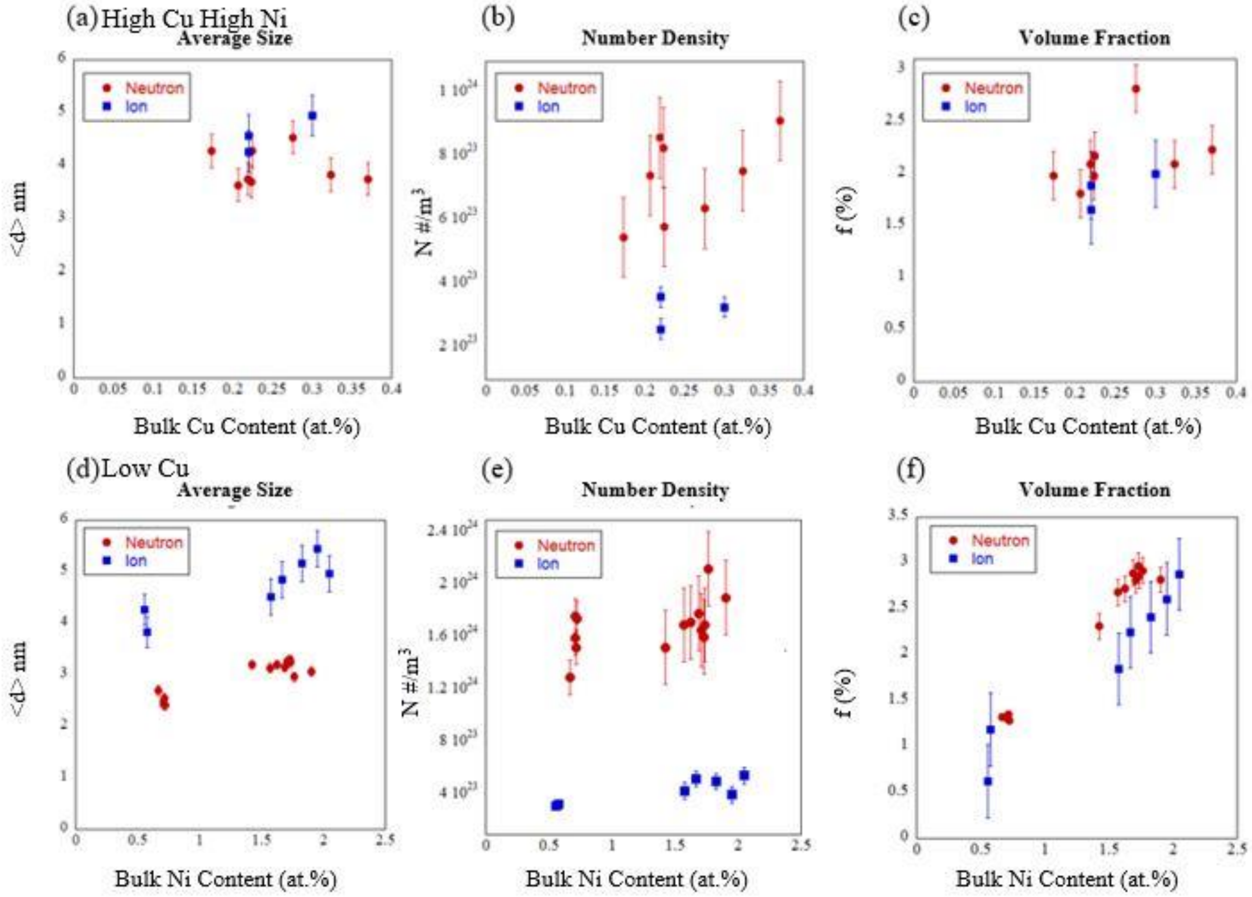

Figure 7. The high dpa CPI (DuET:H) and NI (ATR1) individual tip bulk a-c) Cu; and, d-f) Ni alloy content dependence of the precipitate <d>, N and f.

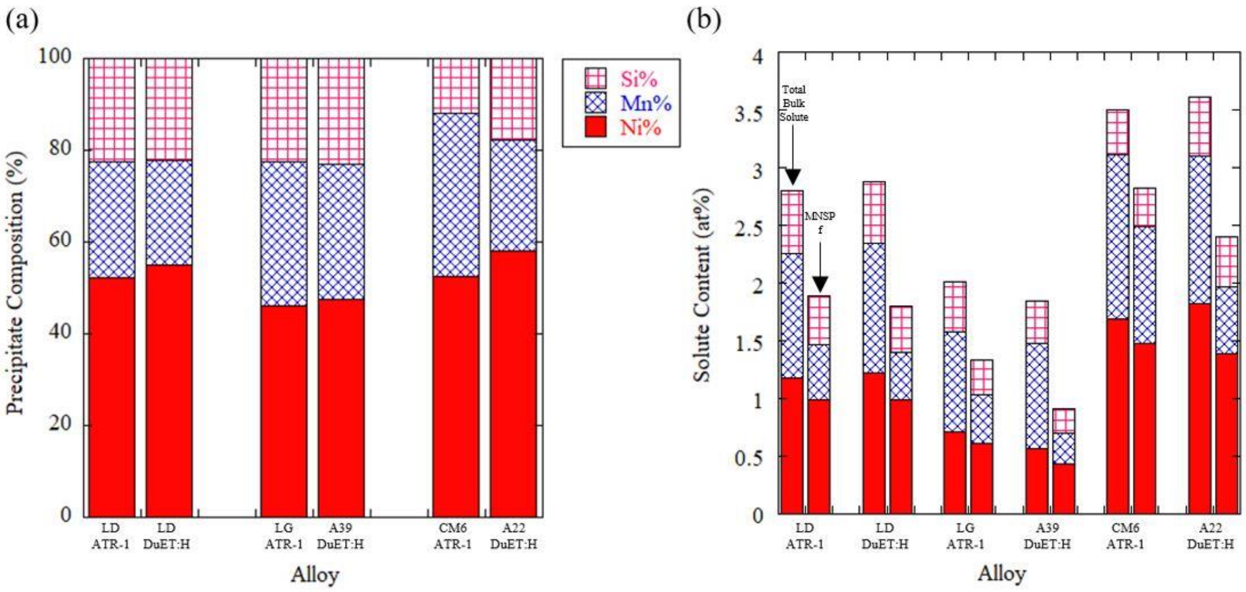

Figure 8. Bar graphs comparing the high dpa CPI (DuET:H) and NI (ATR1) LD and paired medium and high Ni steels: a) the relative Mn, Ni and Si compositions; and, b) the total bulk solute content of the steels (first bar), along with the corresponding precipitate f for the individual solutes (second bar).

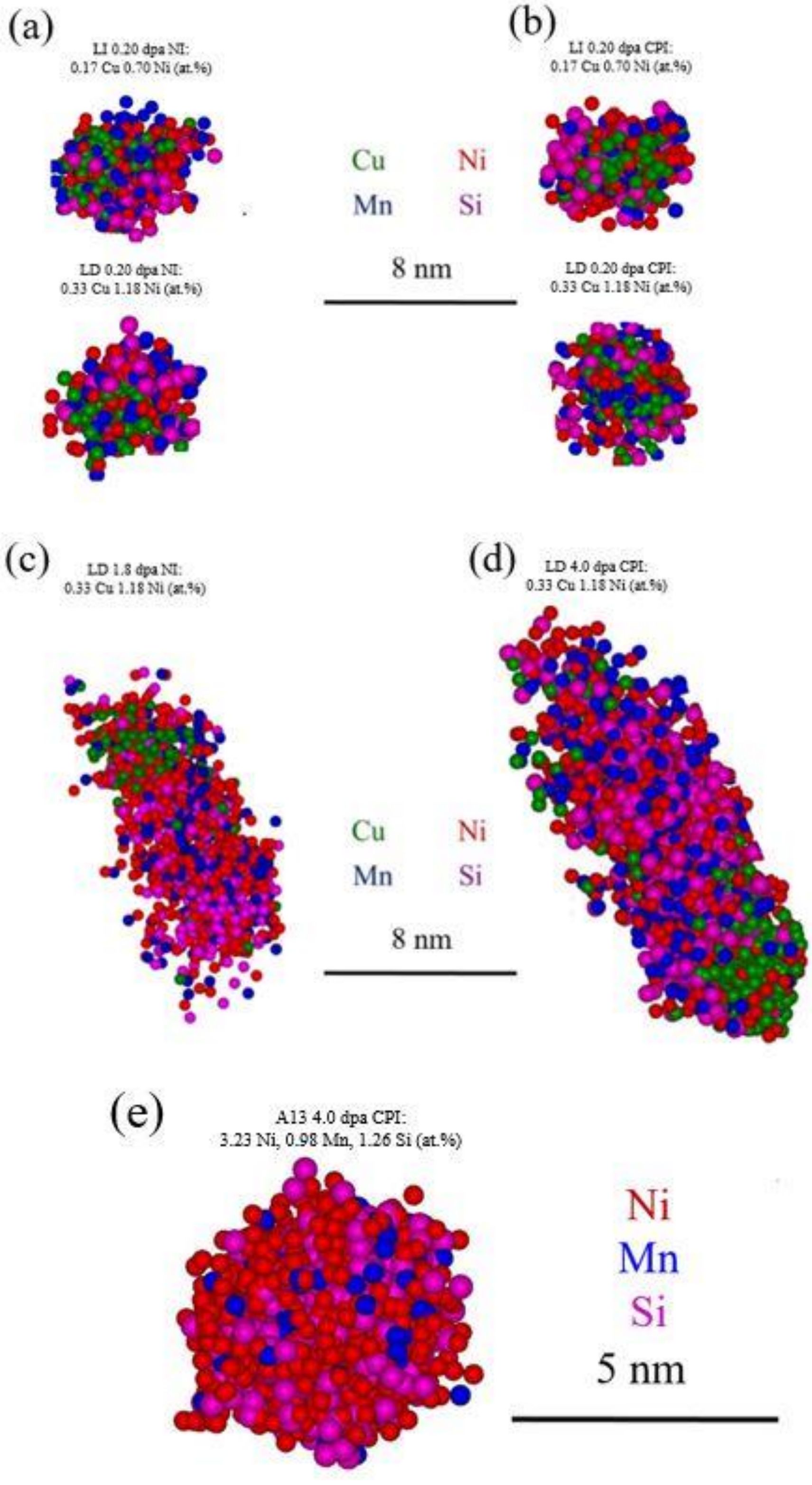

Figure 9. APT maps of the typical Cu-Mn-Ni-Si precipitate in high Cu-Ni content steel (LD) and lower Cu-Ni content steel (LI): a and b) lower dpa BR2 NI and DuET:L CPI; c and d) corresponding APT maps for the same steel (LD) from the high dpa ATR1 NI and DuET:H CPI; and, e) an APT map of a typical polyhedral appearing MNSP in highest Mn, Ni, Si steel (A13) in the DuET:H CPI condition.

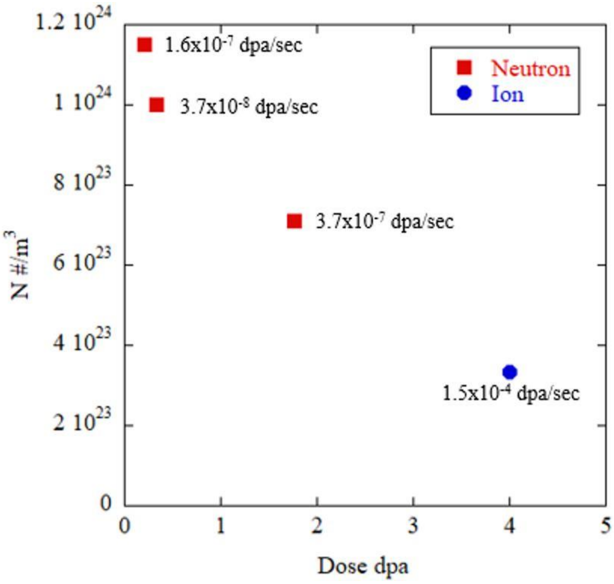

Figure 10. A plot showing that N decreases at higher dpa in the high Cu and Ni steel (LD) for both high dpa rate NI and CPI conditions.

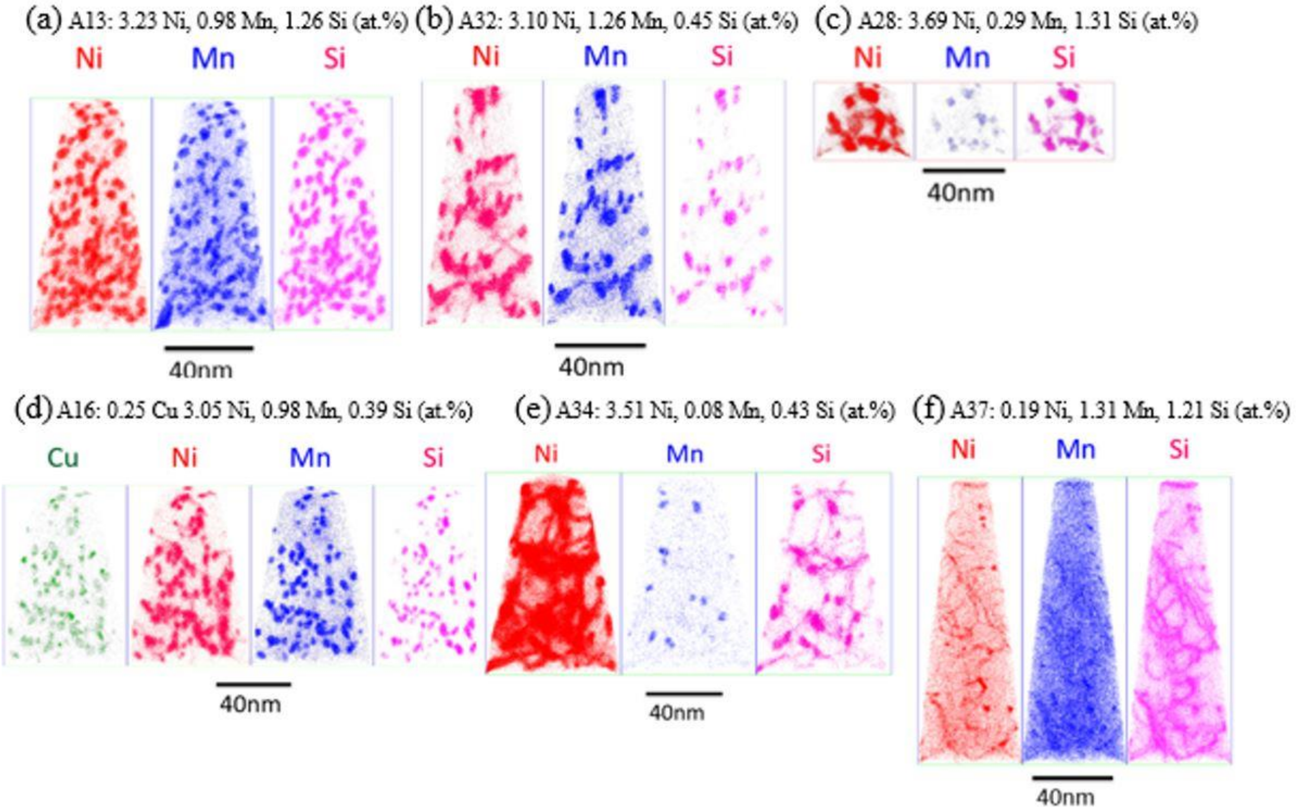

Figure 11. The APT solute maps showing the precipitates formed under CPI (DuET:H) in a) very high Ni and Si, medium Mn A13; (b) very high Ni, medium Si and Mn A32; c) low Mn, very high Ni and Si A28; d) high Cu, very high Ni, medium Mn and Si A16; e) very high Ni with very low Mn content A34; f) low Ni, medium Mn and high Si A37. Except for A16, all of the alloys contain low Cu (<0.05%). All compositions are in at.%.

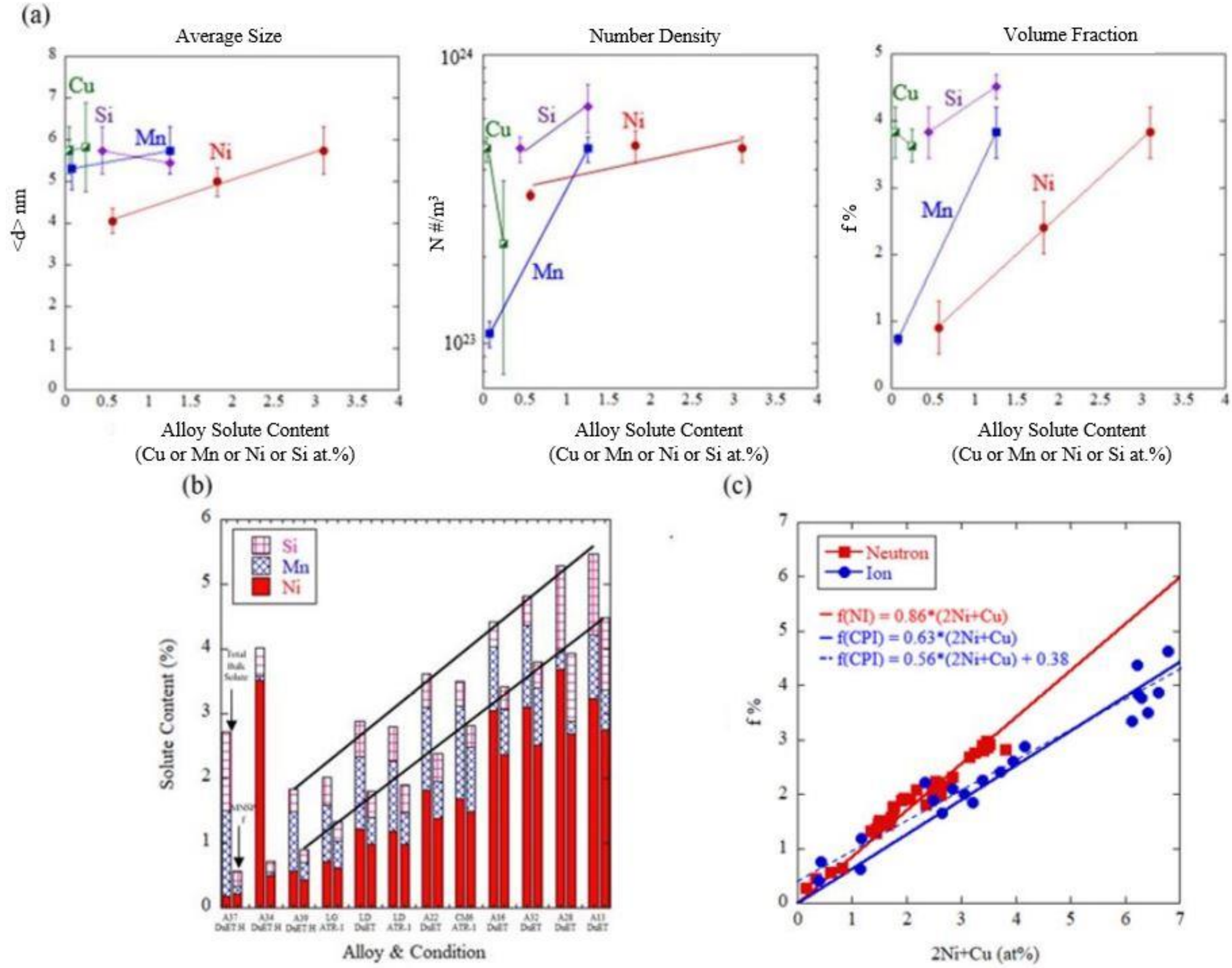

Figure 12. a) Cross plots of the individual effects of variations in alloy solute content of Cu, Mn, Ni or Si (at.%), as shown by the labels in the figure, on <d>, N and f of the MNSPs in alloys with otherwise similar (not identical) compositions; b) stacked bar plots of the total bulk solute content (first bar) and precipitate Mn, Ni and Si f (second bar). c) 2Ni + Cu versus the total f (including Cu) for individual APT tips at high dpa for the NI (red squares) and CPI (blue circles) conditions.

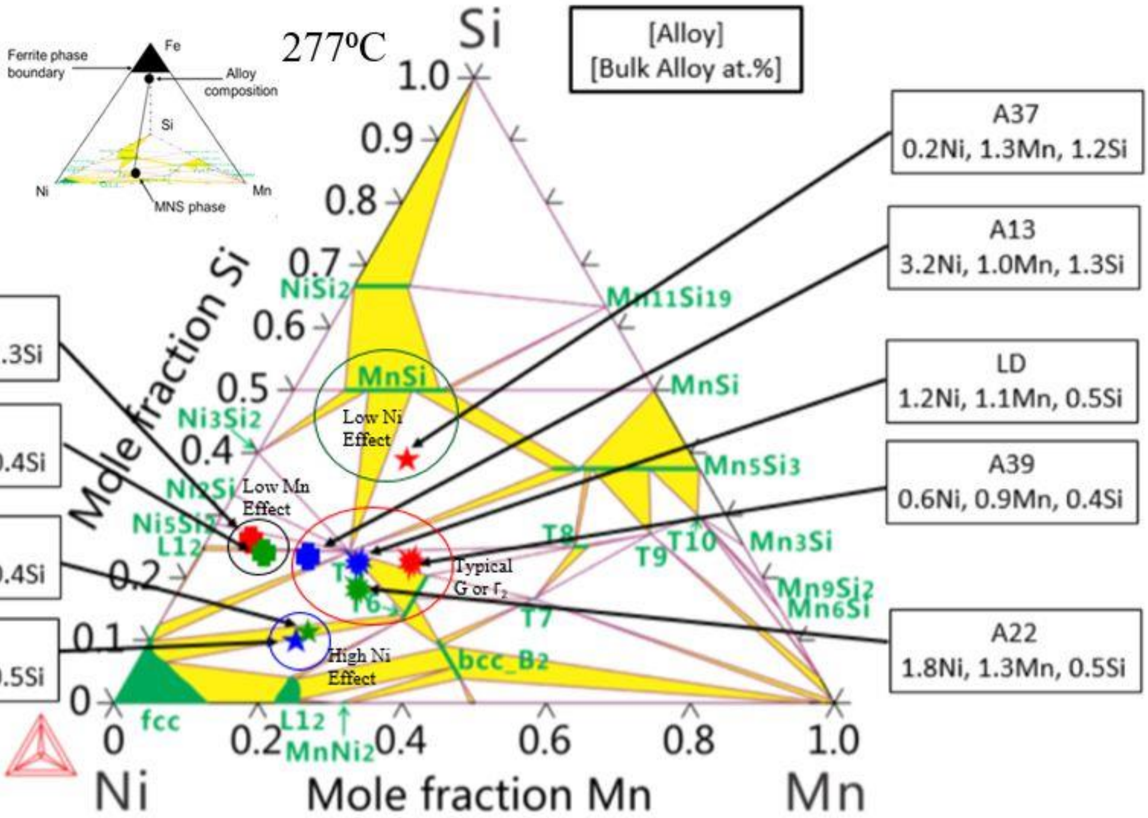

Figure 13. The precipitate compositions for the DuET:H condition plotted on the Mn-Ni-Si ternary projection of the Fe-Mn-Ni-Si phase diagram at 277°C. Alloy composition details are shown outside the ternary [36,37].

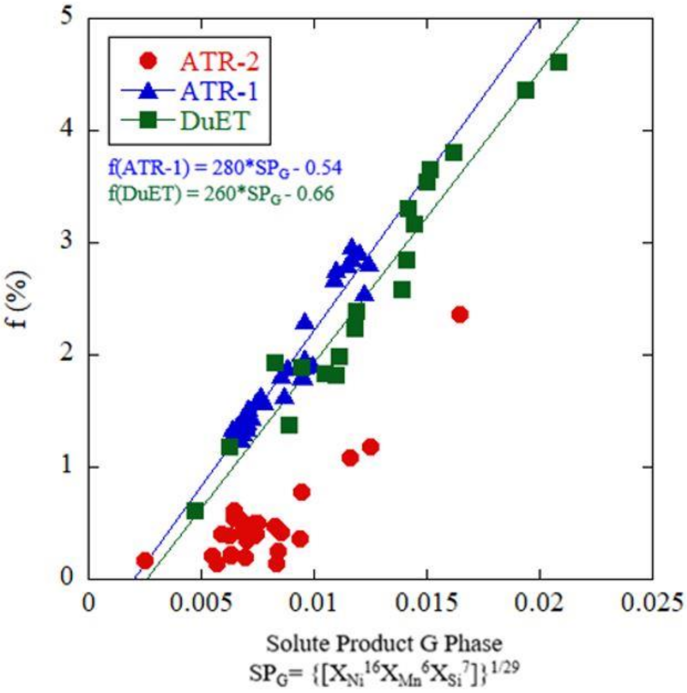

Figure 14: $SP_G$ least square fit to the CPI DuET:H and ATR-1 NI individual APT tip f data. The high dose ATR-1 NI f follow a similar trend, while the lower dose ATR-2 NI f are smaller as expected.

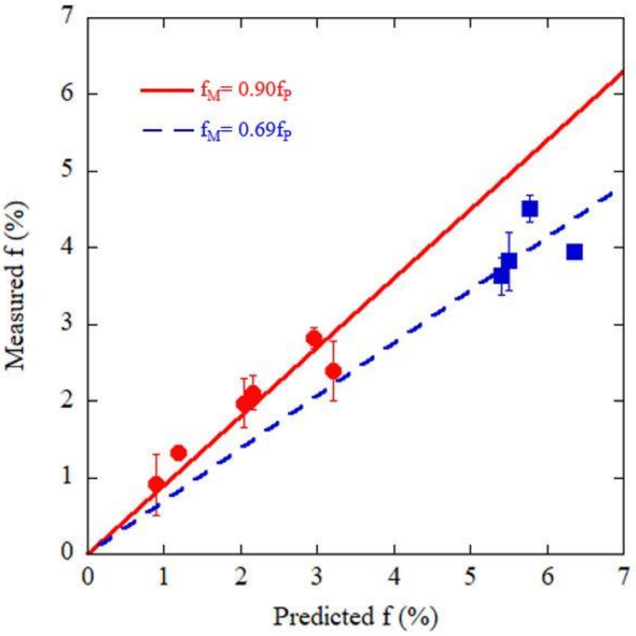

Figure 15. Comparison of the equilibrium thermodynamic model predicted to measured f. The red circles are alloys with sufficient Mn and Si to form stoichiometric G-phases type precipitates with the equilibrium precipitated Ni. The blue squares have insufficient Mn and Si to form stoichiometric G-phases type precipitates consistent with the large amount potentially precipitated Ni. The slopes of < 1 reflect the Gibbs-Thomson effect on the solubility limit in equilibrium with nanoscale precipitates.

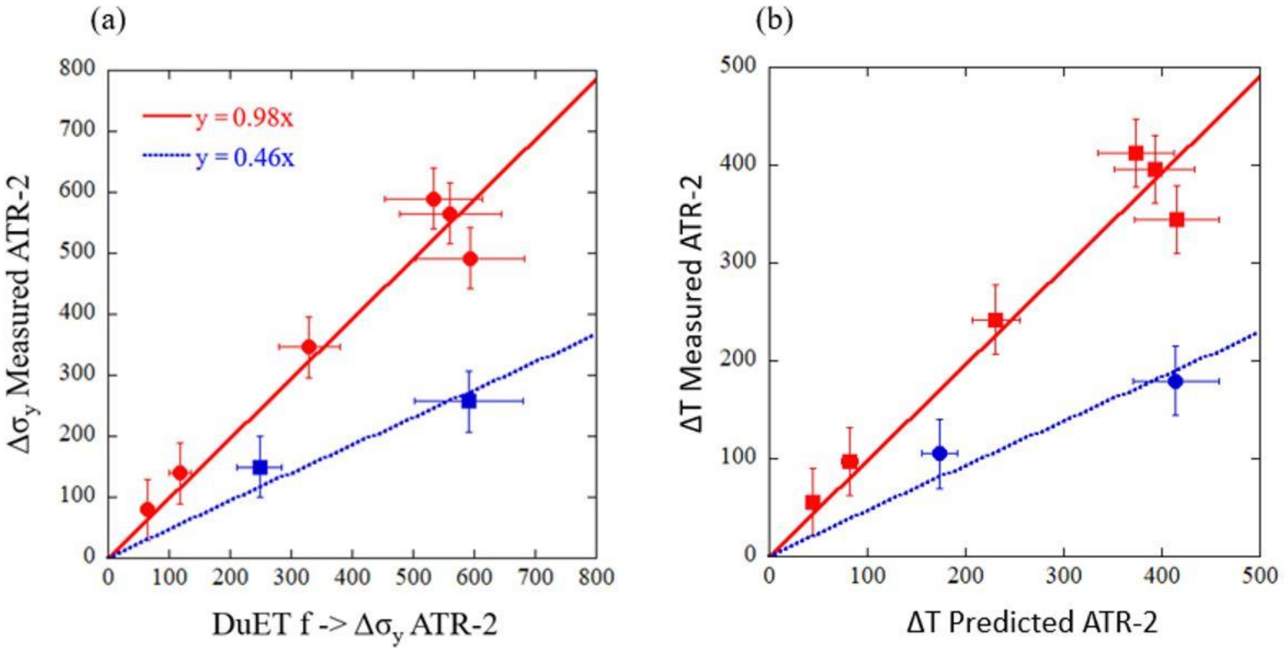

Figure 16. The a) $\Delta\sigma_y$ and b) $\Delta T$ predictions in NI ATR-2 calculated using an empirical adjustment factor plotted against the measured ATR-2 hardening [72]. The filled red symbols are for the alloys that form precipitates with G and $\Gamma_2$ type compositions. The filled blue squares are for high Ni, low to very low Mn steels that form $Ni_{2-3}Si$ type precipitate compositions.

## Supplemental Information

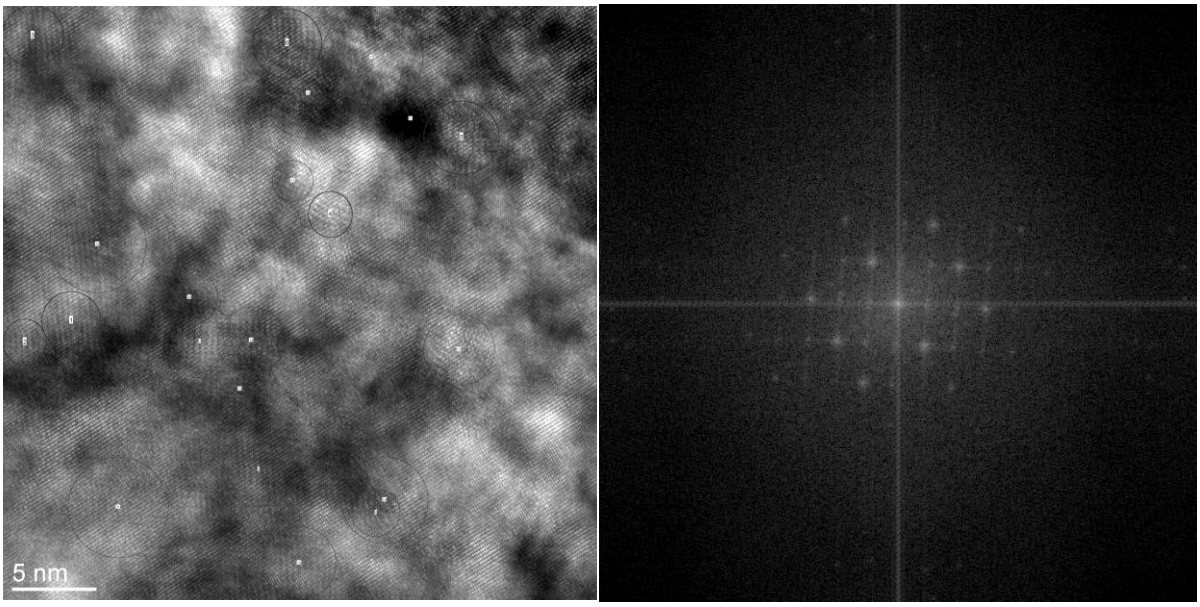

Figure S1. High resolution TEM image and a corresponding FFT image of one MNSP from alloy A28 (3.69at.% Ni 0.29% Mn 1.31%). This power spectra suggests that the MNSP structure is consistent with $Ni_2Si$.